**Continental Shelf Research**
April 2009, Volume 29, Issue 8, Pages 1070-1087
http://dx.doi.org/10.1016/j.csr.2008.11.019




# Temperature variability in the Bay of Biscay during the past 40 years, from an in situ analysis and a 3D global simulation

S. Michel[a, *], A.-M. Treguier[b] and F. Vandermeirsch[a]

[a] Dynamiques de l'Environnement Côtier/Physique Hydrodynamique et Sédimentaire, IFREMER, BP 70, 29280 Plouzané, France
[b] Laboratoire de Physique des Océans, CNRS-IFREMER-IRD-UBO, BP 70, 29280 Plouzané, France

*: Corresponding author : S. Michel, email address : smichel@ifremer.fr

**Abstract:**

A global in situ analysis and a global ocean simulation are used jointly to study interannual to decadal variability of temperature in the Bay of Biscay, from 1965 to 2003. A strong cooling is obtained at all depths until the mid-1970's, followed by a sustained warming over ~30 years. Strong interannual fluctuations are superimposed on this slow evolution. The fluctuations are intensified at the surface and are weakest at ~500 m. A good agreement is found between the observed and simulated temperatures, in terms of mean values, interannual variability and time correlations. Only the decadal trend is significantly underestimated in the simulation. A comparison to satellite sea surface temperature (SST) data over the last 20 years is also presented. The first mode of interannual variability exhibits a quasi-uniform structure and is related to the inverse winter North Atlantic Oscillation (NAO) index. Regarding the vertical structure, most cool and warm anomalies are generated at the surface, with the strongest ones penetrating down to 700 m and lasting up to 5 years. The complete heat budget from 1965 to 2004 is presented, including the contributions of vertical transport, freshwater flux and surface elevation. Interannual anomalies are mainly generated by the surface heat flux, while oceanic transports may become more important at longer time scales.

**Keywords:** Bay of Biscay; Interannual temperature variability; Climatic change; Heat budget; Air–sea flux; Ocean circulation model

## 1. Introduction

During the last decades, the North Atlantic has been warming more rapidly than any other ocean. This relatively small part of the world ocean would be responsible for one third of the global heat content increase from 1955 to 1998 (Levitus et al., 2005). This anomalous heating corresponds to a temperature increase by 0.27°C over the upper 700 m, from 1955 to 2003. The continuous trend is difficult to analyse, because it is superimposed on multi-year oscillations. At regional scales, in situ data are often too sparse to get reliable estimates of long-term changes. Nonetheless, in the Bay of Biscay, many observations sources show strong temperature variations, both in terms of year-to-year oscillations and decade-long trends (Koutsikopoulos et al., 1998; Garcia-Soto et al., 2002, Goikoetxea et al., this issue). However, this interannual variability is not well quantified, its geographic distribution is still largely uncertain and its causes have yet to be identified.

The Bay of Biscay is affected by various physical processes, which act on a wide range of space scales. The Iberian Poleward Current (IPC), flowing from the Spanish north-western corner along the Cantabrian coast, brings warm water during winter, especially during Navidad years (Garcia-Soto et al., 2002). Slope water eddies ("swoddies") are generated above various topographic accidents of the continental slope and carry warm anomalies inside the oceanic region (Pingree and Le Cann, 1992). Considerable river discharges occur along the French coast, creating freshened water plumes which spread over several hundreds kilometres on the wide French shelf (Puillat et al., 2004). Seasonally reversing winds induce upwelling or downwelling-favorable conditions in particular areas of the narrow Spanish shelf (Fontan et al., 2007). Moreover, this semi-enclosed area is connected to the deep ocean, mainly through the North Atlantic Drift, advecting Eastern North Atlantic Central Water (Gonzalez-Pola, 2005). Air-sea heat fluxes also exhibit high interannual variability over this region, in relation with the North Atlantic Oscillation (Cayan, 1992). Because of this complexity, 3D general circulation models are very useful to improve the description of the circulation, as shown by Friocourt et al. (2007).

The purpose of this paper is to document the variability of temperature and heat content in the Bay of Biscay during the last 40 years. Developing a regional model requires a knowledge of the variability at the region boundaries: this information can be provided by basin-scale or global ocean model simulations. Global simulations are available from the DRAKKAR project (Drakkar group, 2007), with a mesh size ranging from 28 km at the equator to 12 km in the Arctic ocean (~1/4° resolution). Regarding in situ observations, a new regional analysis is being developed for the Bay of Biscay (F. Vandermeirsh, personal communication), but a global analysis at coarse resolution

(1°) is already available (World Ocean Database, hereafter "WOD", Levitus et al., 2005). In the present paper, we describe the variability of temperature in the Bay of Biscay, based on both the global model and the global data analysis. Our results provide a basis for future regional analysis and modelling at higher resolution.

After introducing the observational and modelled datasets (section 2), we describe the observed temperature variability and assess the simulation reliability (section 3). The in situ and simulated temperatures are compared with satellite sea surface temperature over the last 20 years. The interannual variability is analysed using empirical orthogonal functions and related to the North Atlantic Oscillation (NAO) index (section 3.4). The in situ analysis and the simulation are used to describe the three dimensional structure of heat content anomalies and their propagation (section 3.5). Then, we compute a complete heat budget from the simulation, in order to estimate how advective processes, surface heat fluxes and turbulent mixing contribute to the heat content variability (section 4).

## 2. Datasets

### 2.1.Global in situ analysis

As a reference, we use the global temperature analysis by Levitus et al. (2005), which was designed to estimate the World Ocean heat content and its decadal evolution. This dataset is based on in situ data of the World Ocean Database 2001, made available by the National Oceanographic Data Center. Approximately 7 millions temperature profiles are included in the WOD01 database and more than 300,000 profiles were added by Levitus et al. Over the global ocean, these measurements were mostly acquired by expandable bathythermographs (XBTs), mechanical bathythermographs (MBTs) and ocean stations (OSD). The remaining data was obtained from moored buoys (MRBs), conductivity-temperature-depth sensors (CTDs), profiling floats (PFLs), bottle samples, etc.

The horizontal resolution of the gridded dataset is 1° and its time period ranges from 1955 to 2003. A pentadal analysis (5-year sampling) is available down to 1500-m, but we use the interannual analysis (1-year sampling) which extends only down to 700 m. Thus, this study is focused on the upper and intermediate layers, from the near-surface (5 m) to the permanent thermocline depth (700 m). Over this depth range, the 3D temperature fields contain 16 levels, with a thickness increasing from 10 meters near the surface to 100 meters below 300 m.

## 2.2.Global simulation

The simulation was designed within the DRAKKAR project (Drakkar group, 2007) and is based on the OPA/NEMO ocean model (Madec, 2008), using a Z vertical coordinate with partial steps and a linearised free surface (Barnier et al., 2006). We use the ORCA025 configuration (hereafter "ORCA"), covering the whole global ocean at a 1/4° resolution. The horizontal grid is tripolar, with 3 pole singularities located over continents, and curvilinear. However, in the Bay of Biscay, the grid lines deviates from latitude and longitude lines by only a few degrees. Thus, the grid spacing is nearly constant, ranging from 16 to 22 km in both directions. The vertical grid is made of 46 vertical levels and contains 22 levels in the upper 700 meters, which are separated by 6 to 107 m.

Constructing surface forcings for multi-decadal simulations of the ocean is a challenge. Atmospheric reanalyses, such as ERA40 from the European Centre for Medium-range Weather Forecast (ECMWF), are burdened by well-known weaknesses regarding radiation and precipitations (Brodeau et al., 2008). We use a strategy proposed by Large and Yeager (2004), implemented in global model intercomparisons by Griffies et al. (2008) and adapted to ERA40 by Brodeau et al. (2008). Radiation is obtained from satellite data, precipitation from a composite product built from in situ and satellite data, and turbulent fluxes are computed using the bulk formulae of Large and Yeager (2004) combined with meteorological variables from ECMWF (air temperature at 2 m, air humidity at 2 m and wind speed at 10 m). One aim of improving atmospheric forcing is to minimize unrealistic relaxation of sea surface salinity towards climatology in models (Griffies et al., 2008); however in ORCA it has been found necessary to keep a relaxation to climatological salinity, with a time-scale of 36 days in the top model layer (6 m), to avoid unrealistic drift in polar regions. River run-offs are provided by a monthly climatology, including 99 major rivers as well as coastal run-off (Dai and Trenberth, 2002). Note that over the Bay of Biscay area, only the Gironde and Loire rivers are explicitly represented in the run-off forcing.

The simulation covers the full duration of the ERA40 reanalysis, from 1958 to July 2002, plus 2.5 additional years using the ECMWF analysis until the end of year 2004. The model outputs are averaged and saved every 5 days. The simulation is initialized in 1958 with the climatology of Levitus (1998) and undergoes substantial adjustment during the first years. For this reason, only the period after 1965 is considered in this paper. Although the simulation is not fully equilibrated (reaching equilibrium on the global scale requires centuries), the model drift in the upper layers of our region of interest seems moderate enough (at least, it does not override interannual variability).

The model resolution does not allow a realistic representation of the Mediterranean water outflow at Gibraltar. Therefore, a relaxation to climatology has been added in the Gulf of Cadiz, in order to prevent temperature and salinity drifts in the Mediterranean water layer (800-1200 m).

This simulation has been designed to study basin-scale variability and global changes, thus it does not resolve all the processes occurring over the continental shelf and slope. For instance, tides are not included in the model physics, so tidal currents, internal tides and associated mixing are not represented. Moreover, the model resolution does not allow to simulate properly coastal currents and cross-slope transfers. In particular, the effects of mesoscale circulation and eddies are parameterised to a large extent by biharmonic viscosity and isopycnal Laplacian diffusion. Recently, Friocourt et al. (2007) have studied the seasonal cycle of circulation in the Bay of Biscay, from a numerical simulation based on the OPA model, with a finer horizontal resolution (~1/15°). Their regional simulation was forced with temperature, salinity and velocities from a North-Atlantic model (Smith et al., 2000). We have verified that the ORCA global simulation represents water mass properties better than this regional simulation, by calculating profiles of temperature and salinity similarly to Friocourt et al., (2007) (their Fig. 2). The bias in deep temperature present in these authors' simulation is absent in ORCA and the properties at the Mediterranean Water level are much more realistic (not shown). The model circulation is compared with Friocourt et al. (2007) in section 4.

### 2.3.Global satellite SST analysis

A satellite data analysis is used to investigate the Sea Surface Temperature variability at high spatial resolution. The PathFinder version 5.0 analysis is based on AVHRR (Advanced Very High Resolution Radiometer) measurements from the NOAA series satellites, providing global fields at a 4 km resolution, for each day from year 1985 to 2006. These SST fields are altered by the vicinity of land, cloud cover and other atmospheric perturbations, what is indicated by a quality flag ranging from 0 (masked) to 7 (good). For our climatic, large-scale analysis, selecting only the best quality data is preferable (K. Caisey, personal communication). Thus, we use the so-called “cloud-screened” version, where only data with a quality flag of 7 are included. Also we use the monthly fields, obtained by averaging all available data within a given month at each grid pixel. Then these monthly fields were averaged for each year, in order to get yearly fields that are truly representative of the annual mean SST. This method is more reliable than using directly the yearly fields from the PathFinder analysis, for which the weight of each month depends on the amount of good quality

data. For instance, in the Bay of Biscay where cloudy conditions prevail during winter months, the PathFinder yearly fields exhibit spurious warm anomalies for particular years.

## 3. Temperature variability

### 3.1.Interannual variations

We analyse the temperature evolution from the observations of the World Ocean Database (1° resolution) and from the ORCA global simulation (1/4° resolution). Annual mean values of temperature have been averaged over a rectangular domain, extending from 43°N to 50°N in latitude and from 15°W to the eastern coastal boundary or 1°W, thus including part of the English Channel (Fig .1). Thus, this domain includes the whole Bay of Biscay and the near Atlantic area to the West. The bathymetry depth ranges from about 200 m over the continental shelf to more than 5000 m over the oceanic plain. This choice aims at investigating local processes in the Bay of Biscay, as well as remote processes occurring in the connected part of the north-eastern Atlantic Ocean. Note that we implicitly separate the decadal and interannual times-scales, by presenting successively the trends (obtained by linear regression) and the annual residuals (obtained by removing the trend from the total anomalies).

Both datasets exhibit a temperature decrease during the first part of the period, followed by a strong warming starting in the mid 1970' s (Fig. 2). These two phases are clearly seen from the surface down to the maximum depth of the interannual WOD analysis (700 m). Over the whole 1965-2003 period, the warming trend dominates down to ~500 m in the observations and down to ~300 m in the simulation (Fig. 3a). In all layers, the warming appears weaker in the simulation than in observations. This warming is highest at 50 m, where the observed trend reaches 0.23°C/decade, equivalent to 0.90°C in 40 years, and the simulated trend reaches 0.10°C/decade, equivalent to 0.42°C in 40 years (Table 1). The observed warming is slightly lower at the surface than at 50 m, suggesting that air-sea heat fluxes attenuate the long-term trend in the surface layer (the uppermost 50 m or so). The simulated warming is roughly constant in the 0-50 m layer, thus the model partially reproduces this attenuation. The near-surface temperature from WOD and ORCA is also consistent with the SST from the PathFinder satellite analysis (Table 2). Over the 1985-2003 period, the PathFinder satellite analysis leads to a SST trend of 0.37°C/decade, close to the value from the WOD in situ analysis over the same period (0.30°C/decade) and consistently higher than in the ORCA simulation (0.22°C/decade) (Table 2). This surface warming rate is very close to the values obtained in the North Sea and Baltic Sea for the 1985-2000 period, from in situ analysis and coastal

daily monitoring (Mackenzie and Schiedek, 2007a,b).

Both the initial cooling and the following warming are related to basin-scale trends of ocean temperature. The subarctic gyre experienced a general cooling centred at 60°N, estimated to -0.13°C at 125 m depth during 1948-85 (-0.04°C/decade) (Levitus et al., 1994). This was caused by a cooling and freshening of Labrador Sea deep waters since the early 1970' s, resulting in a deep water cooling over the entire subarctic gyre (Levitus and Antonov, 1995). However, the cooling could also originate from the subtropical gyre, as a SST decrease was observed over the Gulf Stream area, during the 1950' s and 1960' s (Rayner et al., 2003). After a few years, these cold anomalies would have entered the Bay of Biscay, producing the temperature decrease which culminates around 1975 (Fontan et al., 2007, Goikoetxea et al., this issue). The subsequent warming trend would be related to an increase in air temperature over the whole North Atlantic intergyre area (Perez et al., 2000). In a wider geographic context, the mean temperature increase in the 0-300 m layer of whole North Atlantic is estimated to 0.07°C/decade form 1955 to 2003 (Levitus et al., 2004). The warming is significantly intensified in the Bay of Biscay, where it ranges from 0.09 to 0.23°C/decade in the 0-300 m layer (Fig. 3a).

Strong oscillations are superimposed on the slow trends, with an apparent period of 6 to 10 years (Fig. 2). Such quasi-decadal oscillations were also documented by Levitus et al. (1994) in the North Atlantic Ocean and by Goikoetxea et al. (this issue) in the southeastern Bay of Biscay. Both the observations and the simulation indicate that the oscillations amplitude decreases rapidly with depth, from the surface down to about 400 m (Fig. 3b). The magnitude of the fluctuations is quantified by the standard deviation of annual residuals. At the surface, this RMS residual amounts to 0.33°C in the observations and 0.26°C in the simulation (Table 1). The fluctuation amplitude is divided by a factor two from the surface to the 200-m depth and reaches a minimum at 400 m (0.10° C in WOD and 0.07°C in ORCA). Below the 400-m depth, interannual fluctuations tend to increase significantly in intensity. Thus, these fluctuations are not only forced at the surface, but also generated internally in the intermediate ocean layers. In contrast, the decadal trend decreases quasi-linearly from 50 m down to 600 m in the observations, and even deeper in the simulation (Fig. 3a). This suggests the warming tendency is generated in the mixed layer and counteracts a cooling tendency in intermediate waters.

### 3.2.Comparison between observations and simulation

The previous section has shown the observed trends and fluctuations are in good agreement

with the simulation. To further confront the simulation with the in situ analysis, we compare statistically the two datasets (Table 3). The interannual mean bias (simulation – observations difference) is very low at the surface (lower than 0.02°C). This is expected, since the air temperature used to force the model is itself constrained by the observed SST. The bias is positive in the ENACW, down to ~500 m, and culminates to +0.28°C at 400 m (Fig. 3c). At 600 m, the bias has a similar magnitude but an opposite sign (-0.27°C). This is difficult to interpret, as the bias changes sign again in the Mediterranean Water, around 1000 m (not shown). Thus, the strong cooling obtained at 600 m in the simulation, until the end of the 1970' s (Fig. 2d), may be due to a slow adjustment of water masses, rather than a climatic signal. The bias between satellite and in situ observations is acceptable: the PathFinder SST, available from year 1985, is cooler by 0.23°C than the WOD near-surface temperature, while the simulation temperature is only cooler by -0.1°C over the same period (Table 2).

The RMS difference ranges from 0.20°C in the mixed layer (0 to 100 m) to 0.13°C in the intermediate layers (around 400 m) (Table 3). Thus, as expected, errors are higher in the layers experiencing a stronger variability, but the agreement remains reasonable at all depths. When removing the linear trend, the RMS error on residuals remains around 0.15°C between 100 m and 600 m. Thus, a significant part of the misfit is due to underestimating the warming trend in the simulation. To put these results into perspective, we compare the PathFinder SST to the WOD analysis, during years 1985 to 2003 (Table 2): in this case, the RMS error amounts to 0.12°C, close to the ORCA simulation which leads to an RMS error of 0.13°C.

Interannual variations are well in-phase in the two datasets, as appears from the time series and the correlations (Figs. 2 and 3d, respectively). The time correlation of interannual anomalies ranges from 92% at the surface to 59% in intermediate layers (600 m), except around the 300-m depth, where it falls to less than 50%. Between 400 and 500 m, the correlation is not significant (significativity lower than 95%). As noticed earlier, the simulated temperature at this depth differs considerably from the observations. When comparing the non-linear part of the signals (residuals), the time correlation is slightly lower, ranging from 91% at the surface to 52% at 600 m, except between 300 and 500 m, where it drops to less than 50%. Over the period 1985-2003, the residuals from the PathFinder SST and from the ORCA simulation are correlated at 96% with the WOD near-surface temperature, what proves the robustness of the SST interannual variations (Table 2). When considering the total anomalies, the correlations between PathFinder, ORCA and WOD remain practically unchanged (not shown) because their linear trends are similar and represent a small

proportion of the interannual variability at the surface.

In summary, the time-series of observed and simulated temperatures averaged over the domain are fairly consistent at all depths, from the surface down to 700 m (Fig. 2). The biases between the ORCA simulation and the WOD analysis are lower than ±0.3°C (Fig. 3c) and the RMS differences do not exceed 0.2°C. Interannual variability is well reproduced by the model: the maximum RMS residual reaches 0.26°C near the surface, versus 0.33°C in the observations (Fig. 3b). However, the decadal trends are underestimated by about 50%: the maximum value amounts to +0.10 °C/decade at 50 m, instead of +0.23°C/decade (Fig. 3a). When considering SST, the overall agreement with the in situ data (in terms of bias, error and correlation) is satisfying for both the simulation and the satellite observations (Table 2).

### 3.3.Horizontal distribution of interannual variability

In the following analysis, we consider separately the horizontal distribution of interannual fluctuations (exhibiting a ~6-year period) and long-term tendency (lasting over several decades). We focus on the 100-m depth, which is characteristic of the most variable layer (0-200 m), as shown above.

The trend at 100 m (Figs. 4a and 4c) is positive over the whole domain and decreases in the south-western part. In the WOD observations, the trend and standard deviation are largest in the English Channel, but the resolution is not adequate to study this region in details. Another maximum in the trend is found in the south-eastern corner for WOD, while in the ORCA simulation, the maximum is located over the northern part of oceanic plain. The cooling in the southern part explains why the general warming is underestimated by about 50% in the ORCA simulation (Table 1).

The warming trend in WOD along the Cantabrian slope is consistent with an increasing trend in SST, demonstrated by several studies. Fontan et al. (2007) described a general warming since 1989, particularly in the south-eastern part. Previously, Koutsikopoulos et al. (1998) also noted higher trend values in the south-eastern part and estimated the warming to 0.64°C/decade over the 1972-1993 period. Garcia-Soto et al. (2002) found a warming trend in the Navidad region (offshore the north-western Spanish coast), with a maximum value of 0.75°C/decade from 1976 to 1996. Lavin et al. (1998) showed a warming trend from 1992 to 1995 off Santander, in the Cantabrian sea, estimated to 0.45°C/year at 10 m, but no clear trend at 100 m. Unfortunately, very few long-term observations are available for temperature at depth.

The non-linear anomalies (Figs. 4b and 4d) exhibit a comparable distribution in WOD and ORCA, with a general increase from the deep plain toward shallower areas. In the WOD analysis, a clear maximum appears in the south-eastern corner, similarly to the linear trend (Fig. 4a). In contrast, in ORCA the maximum variability is located over the Celtic and Armorican shelves. A secondary maximum extends along the continental slope in the Navidad region in the simulation, but is not found in the observations. On the contrary, the minimum location roughly coincides in the observations and in the simulation, i.e. in the middle of the oceanic plain.

The lack of a variability maximum offshore of northern Spain in WOD can be explained by the low resolution of the analysis: the narrow Cantabrian shelf is masked on the 1° grid. On the other hand, we think that the absence of the main maximum over the Armorican shelf arises from an insufficient sampling of this shallow area in the database. Indeed, we compared the WOD analysis to a regional analysis with a higher resolution (0.1°) and including 50% of additional data, recently declassified by the French Navy (F. Vandermeirsch, personal communication). In this regional analysis, the temperature variability at 100 m clearly exhibits both a principal and a secondary maxima similar to ORCA. The existence and locations of these two maxima is consistent with Garcia-Soto et al. (2002), who concluded that interannual variations of SST in the Navidad region is highly correlated with the Celtic Sea.

### 3.4.Modes of interannual variability and correlation with NAO

The previous section has demonstrated that interannual fluctuations are well represented in the simulation, whereas decadal trend is less reliable in terms of horizontal distribution and magnitude. Therefore, we now focus on variability at periods of one year to a decade, by removing the linear trend from the time-series. The detrended temperature fields are then decomposed into their main patterns of variability, through an analysis of Empirical Orthogonal Functions. To compare the WOD observations and the ORCA simulation with an independent dataset, we perform the same analysis on the PathFinder satellite SST. The data from the NOAA series satellites are available from 1985, so the overlap period is only 19-year long (1985-2003). Nevertheless, when computing the EOFs over the full 40-year period from WOD and ORCA, similar patterns are obtained (not shown). Also, we extract the EOFs over a larger domain than in the previous sections, in order to reveal the large scale patterns of variability (Fig. 5). The selected domain is twice wider in both directions (28° in longitude and 14° in latitude), but in the Bay of Biscay the resulting patterns are similar with the previous, smaller domain.

In all three datasets, the first EOF exhibits a quasi-uniform distribution, with an enhanced amplitude in the interior of the Bay of Biscay (Figs. 5a,c,e). This pattern is clearly the dominant one, as it represents about 60% of the (non-linear) interannual variability in WOD, ORCA and PathFinder. When performing the analysis over the Bay of Biscay domain (with a ~4 times smaller surface area), the explained variance increases to nearly 80%, because the number of freedom degrees is reduced. Conversely, if we extent the time-series to years 1965-2003 (twice longer), the explained variance decreases to around 50%. In all cases, the spatial pattern of EOF1 remains unchanged in the Bay of Biscay.

The time-series of the first EOF are similar for all three datasets and appear anti-correlated to the NAO index (Fig. 6a), as warm (resp. cool) anomalies often coincide with negative (resp. positive) NAO indices. The correlation between monthly NAO indices (from the Climate Prediction Center) and the annual mean temperature from WOD is most significant for the December index and amounts to -41% over the 1965-2003 period (not shown). Note that over the satellite data period (1985-2003), the correlation with the December NAO index rises to -52% for WOD, -50% for PathFinder and -40% for ORCA. Thus the model reproduces the NAO impact on temperature in this area, although this link is slightly underestimated with respect to observations.

The NAO signature on SST is a tripole over the northern Atlantic basin, with a main pole in the subtropical gyre and two opposite poles at tropical and subpolar latitudes. During positive NAO phases, the subpolar pole appears as a cold SST anomaly centred to the south-west of Iceland, extending south-eastward to the Bay of Biscay (Wu and Liu, 2005). Indeed, positive NAO phases are characterised by a high pressure anomaly over the Azores region, what increases the wind-stress in the Bay of Biscay. This in turn increases the surface heat loss (through latent and sensible heat fluxes) and cools the upper layer. Additionally, along the Cantabrian coast, enhanced north-easterly winds are enhanced in case of positive NAO, which favour upwelling conditions and prevent warm water to be advected northward. Garcia-Soto et al. (2002) found a high correlation between negative NAO and marked Navidad years, when the north-easterly wind-stress relaxes, allowing the Iberian Poleward Current to penetrate further into the Bay of Biscay.

The second EOF appears as an East-west gradient, or coastal/oceanic dipole, in all three datasets (Figs. 5b,d,f), in spite of slight differences. This pattern is of secondary importance compared to EOF1, as it explains about 15% of interannual variance. The time-series of EOF2 are less well correlated than for EOF1 (Fig. 6b), but the mains highs and lows are consistent in each three dataset. In particular, the EOF2 in WOD and ORCA exhibits opposite variations in the 1960' s

and 1970' s, what may be attributed to the absence of satellite data in the forcing dataset before 1980. Three modes are required to describe about 80% of the SST interannual variability from the in situ analysis, while two modes are sufficient for the simulation. The signal is much more complex in the satellite data analysis.

The structure of EOFs is comparable at deeper levels (not shown). The representativity of each EOF varies with depth. For instance, in ORCA, the quasi-uniform pattern of EOF1 at surface becomes the second EOF below 200 m, while the East-west dipole of EOF2 at surface becomes the first EOF. The highest representativity of EOF1 in the upper 200 m suggest an atmospheric origin, consistent with its correlation to the NAO index.

### 3.5.Propagation of temperature anomalies

We now focus on how temperature anomalies, which can be linked to the variability modes described above, penetrate vertically and propagate horizontally. Most non-linear anomalies are concentrated between the surface and the 100-meter depth (Fig. 7) and many are intensified at the surface, suggesting they may be generated by air-sea heat fluxes. For instance, the three coldest anomalies in 1972, 1986 and 1993, as well as the warmest anomaly in 1989, are produced at or near the surface. Meanwhile, the second and the third warmest anomalies occur at subsurface (about 50 m deep), in 1966 and 1997. These warm and cool events are also shown in the time-series of Fig. 2. Although simulated surface anomalies are somewhat weaker than in observations, their timing and penetration depth are similar (Fig. 7b).

The profiles of Fig. 7a confirms the visual impression from Fig. 2 that anomalies have longer time-scales at depth than near the surface. This characteristic is more pronounced in the simulation. Anomalies generally persist between two and five years. In many cases, they seem to propagate downward with time. For example the 1966 warm anomaly starts around 50 m (maximum of 0.58°C) and the 0.2°C warming penetrates down to 300 m in one year. This anomaly persists for 3 more years and reaches 450 m in 1970. Similar propagation occur for 1976-78 and 1991-94 cool anomalies. A warm anomaly is found around 150 m in 1981-82, both in the observations and in the simulation. In contrast with the surface anomalies, this subsurface anomaly is stronger in the simulation: the observed warming of 0.1°C extends from 100 to 200 m, whereas the simulated warming extends from the surface to 400 m. This warm anomaly is caused by an anomalous heat advection from the south-western part domain (see below). From 2002, the warming is general below 100 m in the observations, while the simulation only exhibits a

significant warming between 50 and 200 m. In 2003, a warm surface anomaly (due to an unusually hot summer) combines with the previous deeper anomaly, generating a quasi-uniform warming of the water column in the Bay of Biscay.

The origins of temperature anomalies can also be investigated by describing their zonal and meridional evolution. No clear meridional structure is found in the WOD analysis (not shown), probably due to its low resolution, thus we only show the zonal structures. We focus on the temperature averaged in the 0-200 m layer, where the most intense anomalies occur (Fig. 8). Over this depth range, the warmest anomalies occur in 1966-67, 1989-90 and 1997, while the coolest anomalies occur in 1976-77, 1986 and 1994. These anomalies can be sorted in two types: (1) local generation over the continental shelf and slope, (2) advection from the deep Atlantic plain. Examples of type 1 anomalies are found in 1966-68 and 1985-86. Indeed, the warm anomaly of 1966 lies above the Aquitaine and Armorican shelves, from 45°N to 50°N. However, the simulation suggests that this warming starts in 1965 along the Cantabrian, then is advected from the south-western part of the domain by the Iberian Poleward Current (not shown). This anomaly persists until 1968 in the western central part of the Bay of Biscay. The 1986 anomaly is the coolest in 40 years and starts in 1985 on the south-eastern shelf. It spreads northward all over the Armorican Shelf, the Celtic Shelf and the north-western deep area. It persists over the north-eastern shelves during year 1987. Examples of type 2 anomalies occur in 1972-76 and 1981. The 1970' s cooling consists in two phases: in 1972, a cool anomaly is advected from the south-west, reaching 47°N in the central plain, then decays rapidly; in 1976, a similar but stronger anomaly extends to the North of the domain, then persists for one year above the plain and two years above the shelves. Note that the zonal extension of the 1976 anomaly differs considerably between WOD and ORCA (Fig. 8), because of small scales features that are not resolved in the in situ analysis (not shown). The warm anomaly of 1981-82, centred at about 150 m, clearly originates from the North Atlantic Drift and extends to the middle of the Bay of Biscay. Generally, the strongest surface anomalies, whether they are warm or cool, occur in the eastern part, above or close to the shelf (Fig. 8a).

## 4. Heat balance

As the ORCA simulation leads to a good agreement with in situ observations, in terms of annual anomalies of temperature change, we use it to compute the associated heat budget. The computation domain is the same as previously (43°N-50°N, 15°W-1°W), including the whole Bay of Biscay and its westward extension in the Atlantic. The vertical extent is limited to the upper 800

meters, because there are no observation data below this depth to assess the simulation reliability (the WOD interannual analysis has its deeper level at 700 m). Moreover, the main heat content anomalies are assumed to take place in the surface and intermediate layers. For instance, Levitus et al. (2005) have estimated that 91% of the heat increase in the North Atlantic occurred in the 0-1000 m layer during the past 50 years.

### 4.1.Atmospheric heat fluxes

The Bay of Biscay is a region of weak net heat flux, with its zero isoline usually lying around 45°N in the Eastern Atlantic, depending on the flux dataset (Marshall et al., 1993; Large and Yeager, 2004). The surface heat flux distribution calculated in the ORCA simulation in the Bay of Biscay, includes both positive and negative annual mean values (Fig. 9a). The flux is positive (heat gain to the ocean) in the south-western part, particularly along the western Iberian coast (up to 40 W/m²), where cold upwelled water is warmed at the surface. Positive values are also found in the Celtic Sea, with a much weaker intensity (10 W/m²). The flux is negative (heat loss for the ocean) in the north-western corner (down to -30 W/m² at 50°N/15°W), where surface water is cooled by air from subpolar regions. Weaker negative values (-10 W/m²) are found over the Armorican shelf and offshore the Aquitaine and Cantabrian slopes.

The interannual variability of the surface flux (Fig. 9b) is highest near the north-western corner (up to 12 W/m²), above the North Atlantic Drift. The flux variability is also high over the Armorican Shelf and also along the Cantabrian coast, where SST is essentially controlled by upwelling conditions. In contrast, the surface flux is particularly stable in the south-eastern corner.

Over the whole 1965-2004 period (Fig. 10a), the domain-averaged net heat flux is almost neutral (0.1 W/m²). This mean value essentially results from a high solar radiation (134 W/m²) and strong heat losses through latent flux (-66 W/m²) and thermal radiation (-56 W/m²). The contribution of sensible flux (-12 W/m²) is secondary, although not negligible. The interannual variability of the net heat flux (5.6 W/m²) is produced by a complex combination of all four components, as they all exhibit comparable fluctuations (Figs. 10b,c,d,e). However, the latent heat flux variability is about twice as large the other components.

The net heat flux tends to increase during the whole simulation, with a rate of 0.14 W/m²/year, equivalent to +5.6 W/m² from 1965 to 2004. Quasi-decadal fluctuations result in two cooling periods, until 1975 and during the 1980' s, and two heating periods, first from 1975 to 1980, then from 1990 till the simulation end, with a magnitude about 4 W/m² (Fig. 10a). Interannual

variations produce annual peaks exceeding 10 W/m². The lowest net heat flux occurs in 1986 (-14 W/m²) and is caused by simultaneous weak solar radiation and strong latent heat loss. Conversely, the highest net flux occurs in 1997 (+12 W/m²), due to a maximum solar radiation and a low latent heat loss. Year 1986 also corresponds to the coolest temperature anomaly in the 0-200 m layer (Figs. 2, 8), while year 1997 corresponds to a marked warm anomaly. The 1966 and 1989 warm anomalies coincide with positive heat fluxes and the 1972 cool anomaly coincides with a negative flux, even if the flux values are not exceptional during these years. In contrast, the 1977 and 1993-94 cool anomalies, as well as the 2003 warm anomaly, are associated to surface heat fluxes with opposite signs. Thus, the relation between upper layer temperature and heat flux anomalies in this region is not straightforward. Oceanic processes are probably intense enough to compensate, or even reverse, the effect of air-sea flux fluctuations at the interannual scale.

### 4.2.Simulated circulation in the upper layers

Before describing the heat transport, the modelled circulation needs to be validated. The Bay of Biscay circulation over the shelf and the upper slope is relatively well-known (e.g. Garcia-Soto, 2002), but in deeper layers and further offshore, currents are still poorly sampled. Thus, the ORCA circulation is verified against a regional simulation, performed by Friocourt et al. (2007), hereafter F07. We focus on the seasonal cycle of the simulated circulation, as its seasonal variability is much stronger than its interannual variability, especially over the slopes. Most features of the seasonal circulation obtained in the ORCA simulation are consistent with F07, despite a much lower model resolution. In order to facilitate the comparison between these two simulations, we averaged the current velocities in the same depth range (30-160 m) and at the same phases of the seasonal cycle (Fig. 11). However, our climatological cycle was computed from 40 years, instead of 10 years in F07, and we present monthly means rather than daily snapshots, to get more robust pictures of the circulation.

In the ORCA simulation, the slope current is directed poleward in winter, from Cape Ortegal to the Armorican slope at about 48°N. The poleward flow extends over the Aquitaine shelf and continues northward offshore Brittany. In early spring, the slope current starts reversing in the Cantabrian Sea, but it is still clearly directed poleward from the Basque slope to Goban Spur. In summer and autumn, the slope current flows equatorward, with only a small weakening offshore southern Aquitaine (~2°W). The highest velocities are found along the Iberian slope, with a maximum offshore Cape Ortegal. This westward slope current is connected to the southward

Portuguese Current, as evidenced from observations by Martins et al. (2002). Note that part of this westward flow detaches from the shelf-break and penetrates over the deep plain, then turns southward at about 12°W. This current detachment is even stronger in fall. The simulated seasonal cycle is in qualitative agreement with F07, although the equatorward flow in summer seems stronger. The ORCA circulation along the slope is also qualitatively consistent with observations discussed by Pingree and Le Cann (1990), Colas (2003) and Serpette et al. (2006). The good quality of the simulated currents along continental boundaries is probably due to the numerical schemes improvements discussed by Barnier et al. (2006).

Over the abyssal plain, the monthly mean currents in the upper layer are as strong as along the slopes, but their seasonal variability is much weaker. The main current entering the domain is located between 47°N and 49°N (Pingree, 1993; Paillet and Mercier, 1997). This flow can be seen as an extension of the North Atlantic Drift southern branch or a part of the equatorward recirculation of the subtropical gyre. This eastward current is slightly weaker in winter and oscillates between 45°N and 49°N, with maximum velocities around 48°N. Almost all the flow recirculates south-westward in the Atlantic part (east of 10°W), then exits the domain around 44°N and 14°W. Only a thin eastward vein, located along 45.5°N, penetrates into the Bay of Biscay and reaches the slope. During spring, the eastward current decreases, except in the north-western corner (50°N/15°W). Part of its flow is diverted northward, connecting with the slope current near Goban Spur. Its south-westward recirculation exits the domain more rapidly, mainly at 44.5°N, and its eastward penetration recirculates at 4°W toward the Cantabrian slope. In summer, the NAD flow strengthens between 48°N and 50°N and a second branch appears between 45°N and 46°N. The northern branch divides off Goban Spur (~ 49°N/12°W), either connecting with the equatorward slope current or turning southward, to meet the eastward vein along 45.5°N. The southern branch turns southward, merging with the westward current from the Cantabrian slope, then exits the domain as a wide flow across the southern boundary. In autumn, the eastward flow is concentrated in the northern branch, north of 47°N. Its path along the slope is reinforced with respect to the second path across the plain.

### 4.3.Circulation and heat transports at the domain boundaries

We now consider the time mean flow entering the Bay of Biscay through the domain boundaries (Fig. 12a). The heat transport, integrated vertically from the sea floor, is also represented (Fig. 12b). Only the upper 800 m are shown, because the strongest structures lie in this depth range.

In the following sections, we use loosely the term “heat transport” to designate the transport of temperature referenced to 0°C. The domain averaged temperature could have been used as the reference, but this makes comparisons between different domains and different models more difficult.

At the southern boundary (43°N), heat is advected within the slope under-current carrying Mediterranean Water in the 500-1500 m depth range. This current consists in two veins, as the poleward current is located against the slope during summer and above the western flank of Galicia Bank (11-12°W) during winter. In contrast, the upper slope current in the 0-300 depth range transports heat southward in the annual mean (Fig. 12b). Most heat export across 43°N occurs in the upper 500 m, west of 11°W, as part of the permanent south-westward recirculation. Heat export is also found along the western boundary (15°W), south of 45°N, due to the same circulation feature. Further north, between 45°N and 49°N, heat transport is directed inward the domain in the upper 1000 m, due to the wide and permanent NAD branches. The southern branch (around 45.5°N) carries the largest heat amount and is the deeper one, with a core at about 800 m. The northern branch appears with two cores, as it separates into two veins during winter (not shown). The heat transport associated with these two veins have roughly the same magnitude and they extend down to about 500 m and 400 m, at 47°N and 48°N, respectively. Thus, most heat transport from the Atlantic lies at the depth of the ENACW. Below the northern NAD branch (48.5°N), a narrow eastward current extends downward from 700 m, approximately. At the northern boundary (50°N), heat is essentially exported, within two strong currents at intermediate depth (200 to 1200 m). The major heat export is associated with the northward extension of the northern NAD branch, whose core is located around 14°W and about 800 m deep. A secondary heat export is due to the Celtic slope under-current, centred on the 900 m depth. Above, the upper slope current carries a modest heat amount into the domain, as is it predominantly directed equatorward. Note that the circulation from 1000 to 2500 m, in the depth range of the LSW (Fig. 12a) is in agreement with the currents from the simulation of F07. At the northern boundary, a southward current enters the domain above the lower slope off Goban Spur and at the western boundary, a westward current is found around 45°N, from 1000 to 2000 m.

### 4.4.Mean heat budget in the 0-800 m layer

The model conserves heat, as well as mass, and thus allows the calculation of a regional volume and heat budget. All the terms of the volume and heat budgets in the 0-800 m layer are

presented in Table 4 for the 1965-2004 period. In the study domain, the surface freshwater flux (including river run-offs) is small (~$0.4x10^{-3}$ Sv). This flux is of the same order as the simulated elevation change, which is due to a small imbalance between evaporation and precipitations at the global scale. We have also estimated the input of heat due to the freshwater flux (in the model, the temperature of the precipitations and run-offs is supposed to be equal to the sea surface temperature). Although non-negligible at the global scale (Griffies et al., 2008), this heat input is very small in our domain.

Over the 40-year period, the volume input through the western boundary (3 Sv) is balanced by 2 Sv of northward flow, 0.7 Sv of southward flow and 0.1 Sv of downwelling across the 800 m level (Table 4). Regarding the heat budget, the heat transport across the lateral boundaries consists in a strong import from the west (141 TW), which is redistributed through an export to the North (-90 TW) and a twice weaker export to the south (-45 TW) (see also Fig. 12b).

Over the whole domain, the main heat input is provided by oceanic transports (+1.0 TW) and the main heat loss is caused by temperature diffusion (-1.2 TW) (Table 4). During this particular period, a much lower loss is due to air-sea exchanges (-0.1 TW). The resulting heat deficit produces a heat content decrease within the domain (-0.2 TW). This heat content change is the difference between the beginning of year 1965 and the end of year 2004. The average evolution of the heat content is better represented by its linear trend over the whole period. According to the heat content trend, the simulation leads to a weak cooling of the 0-800 m layer (-7x10-2 TW), due to a negative temperature trend below 300 m (Fig. 3a). This heat content trend corresponds to a domain-averaged temperature decrease of -0.01°C/decade, while observations exhibit a significant increase (+ 0.07°C/decade). The heat balance is subject to strong modulations at decadal and interannual scales, what is demonstrated in the next section.

### 4.5.Heat budget variations over 40 years (1965 to 2004)

The interannual variability of the heat transport ("heat RMS" in Table 4) at the southern boundary is twice lower than at the western and northern boundaries, as shown by the time-series of Fig. 13a. Despite the low mean value of air-sea flux, its interannual variations (3.8 TW) are higher than the total heat transport variations (2.4 TW). Therefore, the heat content interannual variations are primarily due to exchanges with the atmosphere and secondarily to exchanges with the surrounding ocean.

Time-series of transports integrated across each three boundaries and in the 0-800 m upper

layer are presented (Fig. 13.a). The transports at the western and northern boundaries are rather high during the 1970' s and 1980' s, then decrease during the 1990' s (see also Table 5). This decadal evolution may be associated with a deceleration of the North Atlantic subtropical gyre, which feeds the NAD and its eastward extension toward the Bay of Biscay. The transport at the southern boundary only exhibits a significant increase in the late 1970' s and early 1980' s. Generally, both the northern and southern transports are anti-correlated with the western transport (correlations of -89% and -41%, respectively, significant at 99%), because of the horizontal recirculations. While horizontal and vertical heat transports exhibit large interannual variability, the net transport seems to vary on longer time scales (Fig. 13b).

The heat balance fluctuates considerably in the course of the 40-year long simulation (Fig. 13c). The total heat transport decreases regularly since the end of the 1970' s (Table 5). The air-sea flux increases steadily over the 40 years, becoming positive during the 1995-2004 decade. This decadal trend is masked by interannual variability in Fig. 13c, but is evidenced by the 5-year smoothing in Fig. 10a. As a result, the heat content trend switches from a strongly negative value during the first decade (-1.9 TW) to a lower, but significant, positive value during the three following decades (+0.42 TW on average from 1975 to 2004). This is consistent with the domain-averaged temperature from in situ observations (Figs. 2, 7). The warming phase is not continuous over the last 30 years: a slight cooling is obtained during the 1985-94 decade and the warming is twice stronger during the 1975-84 decade than during the 1995-2004 decade.

In addition to these slow trends, several extreme events are worth notifying. The highest total transport values are found from 1978 to 1990. The transport term becomes negative (heat export) only during a few years, due to either a decrease in the westerly import (in 1993 and 2000) or an increase in the northward export (in 1976 and 2003). The highest values of air-sea flux are found during the last decade of the simulation (in 1994, 1997 and 2002), consistently with the increasing trend, and a few weaker positive peaks occur during the previous decades (in 1966, 1977 and 1981). Years 1966, 1997 and 2003 (one year later) correspond to some of the warmest anomalies in the 0-200 m layer (Fig. 8), thus likely to be forced by an anomalous heating from the atmosphere. On the other hand, years 1977 and 1994 correspond to marked cool anomalies, so they cannot be generated by the atmospheric flux. The most negative values of air-sea flux occur in 1986, 1996 and 1969 (in decreasing order). Thus the 1986 cool anomaly, the lowest of temperature anomaly in the 0-800 m layer (Fig. 7), would originate from a strong heat loss to the atmosphere. In 1969, the negative flux anomaly is partly compensated by a positive transport anomaly, so the upper

layer does not cool significantly. In 1996, the heat transport is very weak, thus the heat content change exhibits ones of its lowest anomalies. However, the 0-100 m layer warms during this year, probably because of an increased heat transport within the IPC, associated with the marked Navidad event in 1996 (section 4.1).

At interannual scale, the lateral transport is anti-correlated to the vertical transport (correlation = -87%, significant at more than 99%), thus most heat anomalies transported across the lateral boundaries are advected to deeper layers. The total transport is partially anti-correlated to the air-sea flux (correlation = -34%, significant at 97%), so part of the anomalies advected into the domain by lateral and vertical currents are evacuated at the surface toward the atmosphere (and conversely). However, the total transport is not the main driver of the interannual heat content variations, as both terms are only weakly correlated (correlation = 30%, significant at 94%). The surface flux is more strongly correlated with the heat content variations (correlation = 68%, significant at more than 99%), so interannual temperature fluctuations in the 0-800 m layer are essentially controlled by air-sea exchanges.

## 5. Conclusions

The DRAKKAR model, in its global ORCA configuration with at 1/4° resolution, reproduces surprisingly well the interannual to decadal variability of temperature in the Bay of Biscay. At decadal time scales, the Bay of Biscay experienced a cooling phase until the mid-1970' s, followed by a continuous warming. The simulation reproduces correctly these two phases, even if the rates of change are underestimated. The simulation interannual variability is well correlated with the WOD observations at the surface. The correlation is still significant and high (> 60%) down to the 200 m depth. This demonstrates that the DRAKKAR global model is suitable to provide boundary conditions for regional models, aimed at studying interannual to decadal variability in areas closer to the coast. The most problematic issue remaining for the Bay of Biscay is probably the representation of the Mediterranean Water. This water mass is better characterised in the ORCA simulation than in the simulations of Smith et al. (2000) and Friocourt et al. (2007). However, this performance has been achieved with an artificial relaxation to a climatology in the Gulf of Cadiz, which makes it difficult to represent the interannual variability of the Mediterranean Water.

The WOD global analysis (Levitus et al., 2005), although coarse in resolution, allows to describe the first mode of temperature variability in the Bay of Biscay at interannual to decadal time scales, because this first mode is a large-scale one, correlated with the NAO. The EOF analysis of

the WOD dataset is consistent with the SST from the PathFinder satellite data. The WOD analysis has also allowed us to describe for the first time the vertical structure of the temperature anomalies in the Bay of Biscay. Most anomalies are intensified in the upper 200 m and propagate downward and a few ones seem to be generated at intermediate depths (200 m or deeper). The time scale of anomalies is shorter near the surface and increases at depth. Our attempt to characterise higher EOF modes and lateral propagations is limited by the coarse resolution of the WOD dataset, which does not resolve the high variability present along the Cantabrian slope (such as Navidad events), or on the continental shelves.

The ORCA simulation has been used to estimate a heat balance for the Bay of Biscay, in the upper 800 m and during the last 40 years. The horizontal heat transport has to be considered jointly with the vertical transport, as lateral convergence is compensated by downwelling. In the simulation, the interannual variability of heat content is mostly driven by the local air-sea flux, and to a lower degree by advection. At decadal and longer time scales, the heat balance is more complex: the surface flux may play a damping role at these time scales. We find a large increase in the surface heat flux over the last decade (indeed, the flux produces is a net heating of 1.6 TW during the 1995-2004 decade, while it produces a cooling of -0.7 TW over the three previous decades). This increase in heat flux is partly compensated by a decrease of the heat convergence into the domain, which becomes close to zero (-0.2 TW during 1995-2004). The model-derived heat budget must of course be regarded with caution, considering the underestimation of the recent warming trend by the simulation. Efforts are under way to develop regional modelling at higher resolution, in order to examine the issue of coastal ocean warming in more details.

**Acknowledgements**

We thank the DRAKKAR project team for providing with outputs of the ORCA simulation. The model outputs are available on request and additional information on the simulation can be found on the project webpage: http://www.ifremer.fr/lpo/drakkar/index.htm. The ORCA025-G70 simulation was carried out by Jean Marc Molines (CNRS, LEGI, Grenoble) with the computing resources of the IDRIS CNRS centre (Orsay, France). We also thank the NODC/NOAA for providing the in situ temperature analysis from the World Ocean Database and the PathFinder v5.0 analysis of satellite sea surface temperature. Both datasets are freely available from these webpages: http://www.nodc.noaa.gov/OC5/DATA_ANALYSIS/heat_intro.html and http://www.nodc.noaa.gov/SatelliteData/pathfinder4km. . This work was funded by a grant by

Agence Nationale de la Recherche, through the CHALOUPE programme coordinated by IFREMER.

**References**


Barnier, B. and the DRAKKAR group, 2006. Impact of partial steps and momentum advection schemes in a global ocean circulation model at eddy permitting resolution. *Ocean Dynamics*, 56: 543-567.

Brodeau, L., Barnier, B., Treguier, A.M., Penduff, T., Gulev, S., 2008. An ERA40-based atmospheric forcing for global ocean circulation models. *Submitted to Ocean Modelling*.

Cayan, D.R., 1992. Latent and Sensible Heat Flux Anomalies over the Northern Oceans: Driving the Sea Surface Temperature. *Journal of Physical Oceanography*, 22, 859–881.

Colas F., 2003. Circulation et dispersion lagrangiennes en Atlantique Nord-Est. Ph-D. thesis, 266 pp. Université de Bretagne Occidentale, Brest, France.

The DRAKKAR group, 2007. Eddy-permitting ocean circulation hindcasts of past decades. *CLIVAR exchanges*, 42. (vol. 12, no. 3), 8-10.

Dai, A., Trenberth, K.E., 2002. Estimates of freshwater discharge from continents: latitudinal and seasonal variations. *Journal of Hydrometeorology*, 3, 660-687.

Fontán, A., Valencia, V., Borja, Á., Goikoetxea, N., 2007. Oceano-meteorological conditions and coupling in the southeastern Bay of Biscay, for the period 2001–2005: A comparison with the past two decades. *Journal of Marine Systems*, in press, available online 3 December 2007. doi:10.1016/j.jmarsys.2007.08.003.

Friocourt, Y., Levier, B., Speich, S., Blanke, B., Drijfhout, S.S., 2007. A regional numerical ocean model of the circulation in the Bay of Biscay. *Journal of Geophysical Research-Oceans*, 112 (C9), C09008.

Garcia-Soto, C., Pingree, R.D., Valdés, L., 2002. Navidad development in the southern Bay of Biscay : climate change and swoddy structure from remote sensing and in situ measurements. *Journal of Geophysical Research*, 107 (C8): 28-1 -28-29.

Goikoetxea, N., Borja, A., Fontán, A., González, M., Valencia, V., this issue. Trends and anomalies in Sea Surface Temperature, observed over the last 60 years, within the southeastern Bay of Biscay. *Continental Shelf Research*.

Griffies S.M., A. Biastoch , C. Boning, F. Bryan, G. Danabasoglu, E.P. Chassignet, M.H. England, R. Gerdes, H. Haak, R.W. Hallberg, W. Hazeleger, J. Jungclaus, W.G. Large, G. Madec, A. Pirani, B.L. Samuels, M. Scheinert, A. Sen Gupta, C.A. Severijns, H.L. Simmons, A.M. Treguier, M. Winton, S. Yeager, J. Yin, 2008. Coordinated Ocean-Ice reference experiments (COREs). *Ocean Modelling*, in revision.

Koutsikopoulos, C., Beillois, P., Leroy, C., Taillefer, F., 1998. Temporal trends and spatial structures of the sea surface temperature in the Bay of Biscay. *Oceanologica Acta,* 21, 2: 335-344.

Large, W., Yeager, S., 2004. Diurnal to decadal global forcing for ocean and sea-ice models: the datasets and flux climatologies. *NCAR technical note*, NCAR/TN-460+STR, CGD division of the National Center for Atmospheric Research. Available on the GFDL CORE website.

Large, W.G., 2007. CORE forcing for coupled ocean and sea-ice models. *Flux News, newsletter of the WCRP workgroup on surface fluxes*, 3, 2-3, January 2007.

Lavin, A., Valdés, L., Gil, J., Moral, M., 1998. Seasonal and inter-annual variability in properties of surface water off Santander, Bay of Biscay, 1991-1995. *Oceanologica Acta*, 21, 2: 179-190.

Levitus, S., Antonov, J.I., Boyer, T.P, 1994. Interannual variability of temperature at a depth of 125 meters in the North-Atlantic ocean. *Science*, 266 (5182), 96-99.

Levitus, S., Antonov, J., 1995. Observational evidence of interannual to decadal-scale variability of the subsurface temperature-salinity structure of the world ocean. *Climatic Change*, 31 (2-4): 495-514.

Levitus, S., Conkright, M.E., Boyer, T.P., O' Brien, T., Antonov, J., Stephens, C., Stathoplos, L., Johnson, D., Gelfeld, R., 1998. World Ocean Database 1998a, Volume 1: Introduction. *NOAA Atlas NESDIS 18*, U.S. Government Printing Office, Washington, D.C., 346 pp.

Levitus, S., Antonov, J., Boyer, T., 2005. Warming of the World Ocean: 1955-2003. *Geophysical Research Letters*, 32: L02604.

Mackenzie, B. R., Schiedek, D., 2007. Daily ocean monitoring since the 1860s shows record warming of northern European seas. *Global Change Biology*, 13, 7, 1335-1347 .

Mackenzie, B. R., Schiedek, D., 2007. Long-term sea surface temperature baselines-time series, spatial covariation and implications for biological processes. *Journal of Marine Systems*, 68, 3-4, 405-420.

Madec, G., 2008. NEMO ocean engine. *Note du Pôle de Modélisation*, Institut Pierre-Simon Laplace, France, No 27, ISSN No 1288-1619.

Marshall, J.C., Nurser, A.J.G., Williams, A.G., 1993. Inferring the subduction rate and period over the North Atlantic. *Journal of Physical Oceanography*, 23, 1315-1329.

Martins, C.S., Hamann, M., Fiúza, A.F.G., 2002. Surface circulation in the eastern North Atlantic, from drifters and altimetry, *Journal of Geophysical Research*, 107 (C12), 3217.

Paillet, J., Mercier, H., 1997. An inverse model of the North Eastern Atlantic general circulation and

thermocline ventilation. *Deep Sea Research-part I*, 44, 1293-1328.

Perez, F.F., Pollard, R.T., Read, J.F., Valencia, V., Cabanas, J.M., Rios, A.F., 2000. Climatological coupling of the thermohaline decadal changes in Central Water of the Eastern North Atlantic. *Scientia Marina*, 64, 3, 347-353.

Pingree, R.D., Le Cann, B.,1990. Structure, strength and seasonality of the slope currents in the Bay of Biscay region. *Journal of Marine Biology*. Ass. U.K., 70, 857-885.

Pingree, R.D., Le Cann, B., 1991. Three anticyclonic Slope Water Oceanic eDDIES (SWODDIES) in the Southern Bay of Biscay in 1990. *Deep Sea Research*, 39, 7/8: 1147-1175.

Pingree, R.D., Le Cann, B., 1992. Anticyclonic eddy X91 in the southern Bay of Biscay region, May 1991 to February 1992. *Journal of Geophysical Research,* 97 (C9): 14,353-14,367.

Puillat, I., Lazure, P., Jegou, A.M., Lampert, L., Miller, P.I., 2004. Hydrographical variability on the French continental shelf in the Bay of Biscay, during the 1990s. *Continental Shelf Research*, 24, 10, 1143-1163.

Rayner, N.A., Parker, D.E., Horton, E.B., et al., 2003. Global analyses of sea surface temperature, sea ice, and night marine air temperature since the late nineteenth century. *Journal of Geophysical Research-Atmospheres*, 108 (D14), 4407.

Serpette A., Le Cann, B., Colas, F., 2006. Lagrangian circulation of the North Atlantic Central Water over the abyssal plain and continental slopes of the Bay of Biscay: description of selected mesoscale features. *Scientia Marina*, 70S1, 27-42.

Smith, R.D., Maltrud, M.E., Bryan, F.O., Hecht, M.W., 2000. Numerical simulation of the North Atlantic Ocean at 1/10°. *Journal of Physical Oceanography*, 30, 1532-1561.

Wu, L., Liu, Z., 2005. North Atlantic Decadal Variability: Air–Sea Coupling, Oceanic Memory, and Potential Northern Hemisphere Resonance. *Journal of Climate*, 18, 331–349.

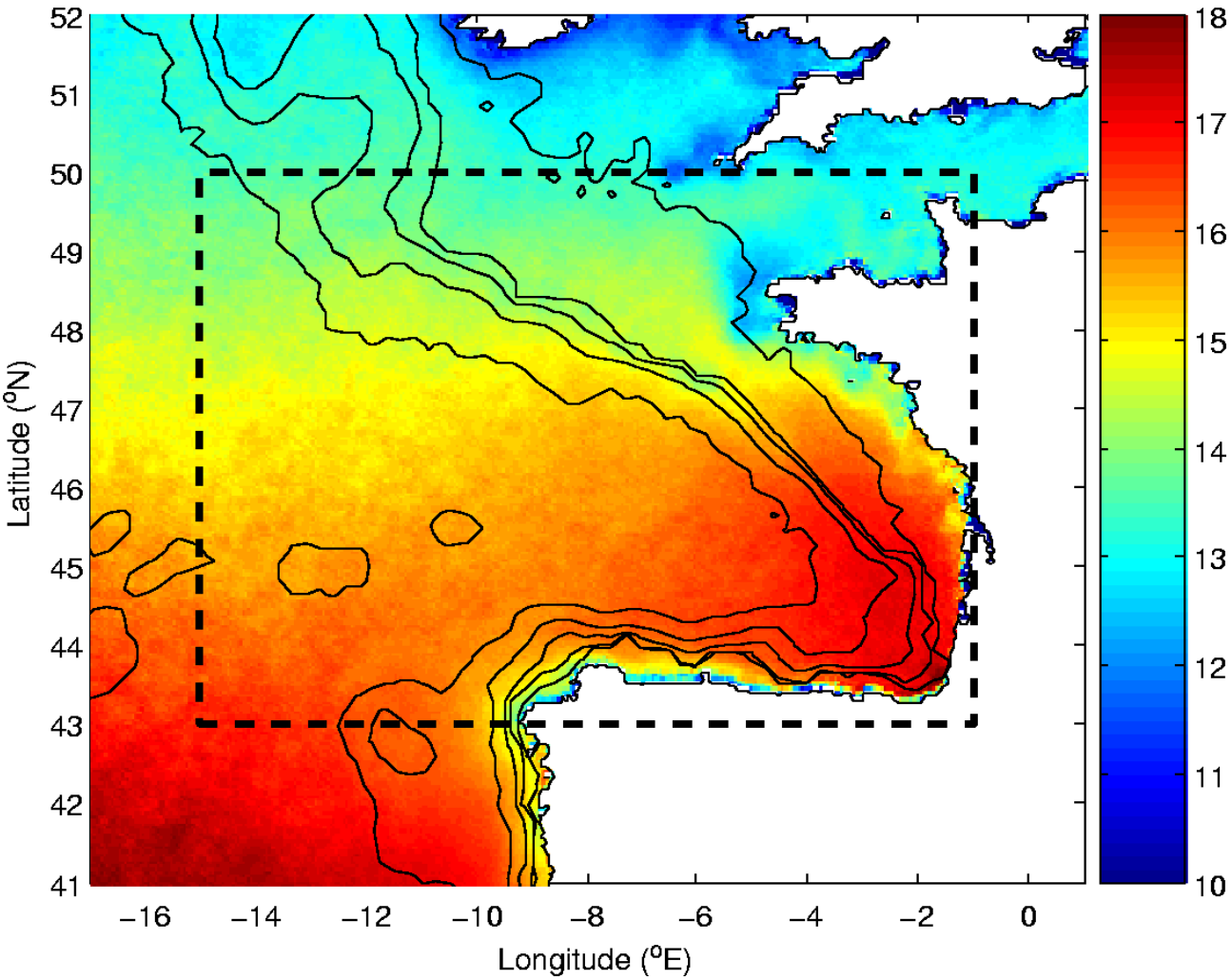


Fig. 1. Sea Surface Temperature (in °C) from the PathFinder v5.0 satellite analysis, interannual mean of years 1985 to 2004 (night-time data). The horizontal resolution is 0.1°. The black lines represent the 100, 200, 800, 2000 and 4000 m isobaths. The dashed rectangle is the domain over which all analyses are performed in this paper: 43°N to 50°N in latitude, 15°W to 1°W in longitude.

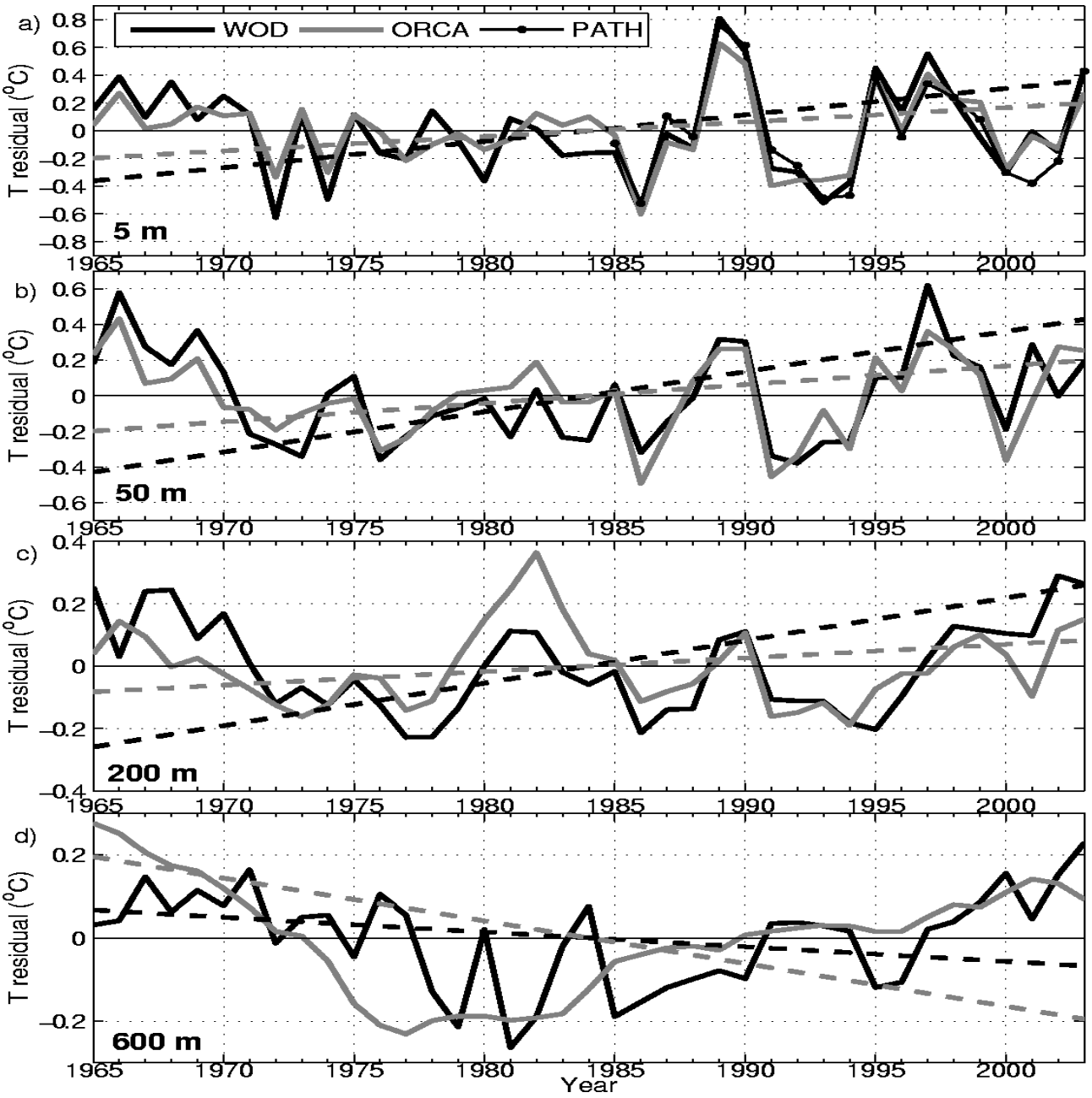


Fig. 2. Time-series of interannual temperature anomalies, for years 1965 to 2003, averaged horizontally over the domain 43-50°N / 15°W-1°W. Four typical levels have been chosen: (a) near-surface (5 m), (b) mixed layer (50 m), (c) thermocline base (200 m) and (d) intermediate water (600 m). Black lines: World Ocean Database, grey lines: ORCA simulation, full lines: residuals (i.e. anomalies with the trend removed), dashed lines: linear trends (significant to more than 95%). In the top frame, the thin line with dots represents SST from the PathFinder satellite analysis (starting in 1985).

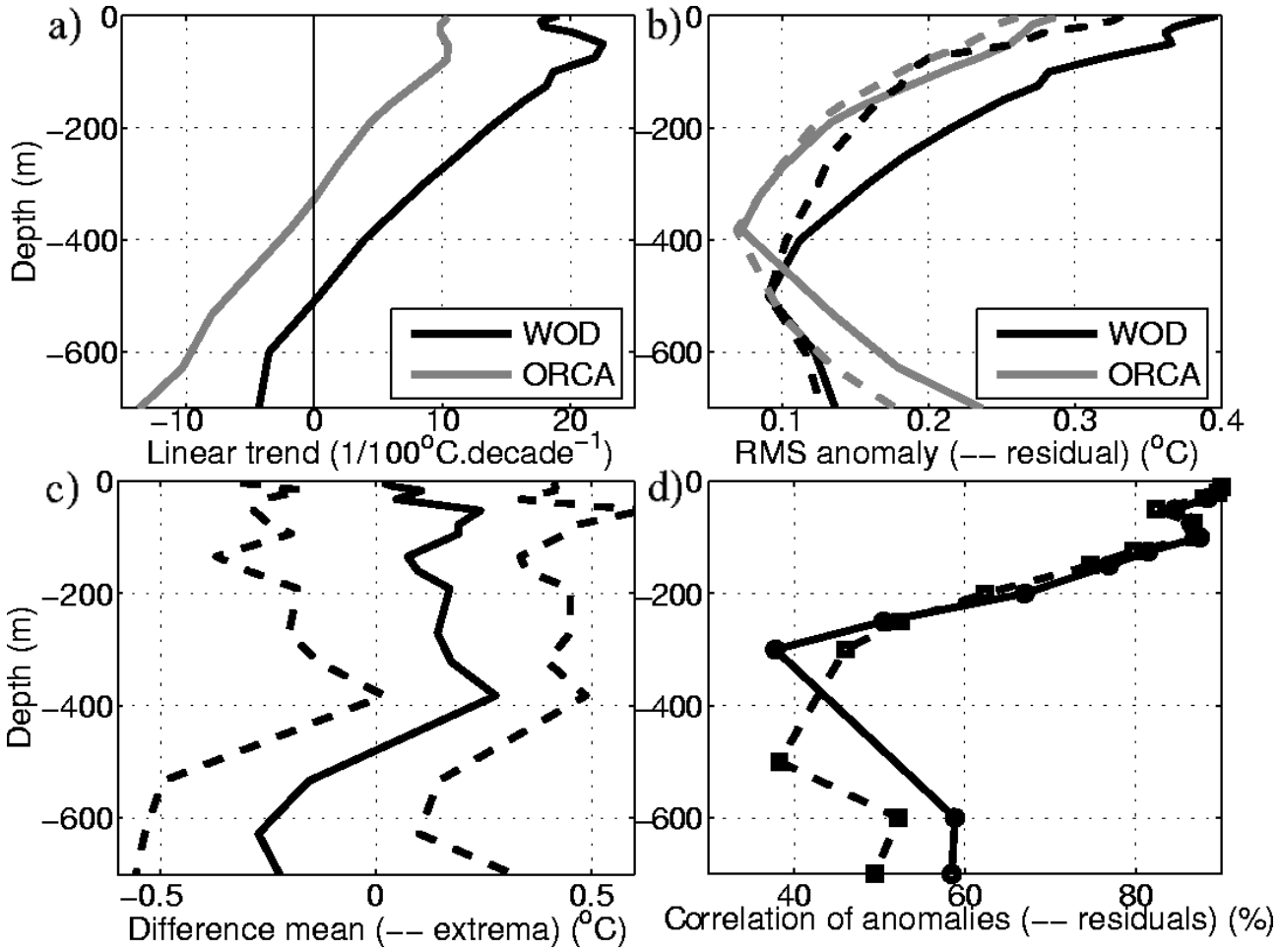


Fig. 3. Vertical profiles of statistics on temperature annual means, for the same data as in Fig. 2. (a) linear trend (in $10^{-2}$ °C per decade, significant to more than 94%); (b) RMS of anomalies (full lines) and residuals (dashed lines); (c) simulation minus observations difference mean (full line) and extrema (dashed lines); (d) correlation between WOD and ORCA for total anomalies (full line) and residuals (dashed line), only at depths where correlation is significant at more than 95% (represented with circles and squares). Black lines represent the World Ocean Database and grey lines, the ORCA simulation. Part of the profile values are given in Table 1 (for Figs. 3a and 3b) and Table 2 (for Figs. 3c and 3d).

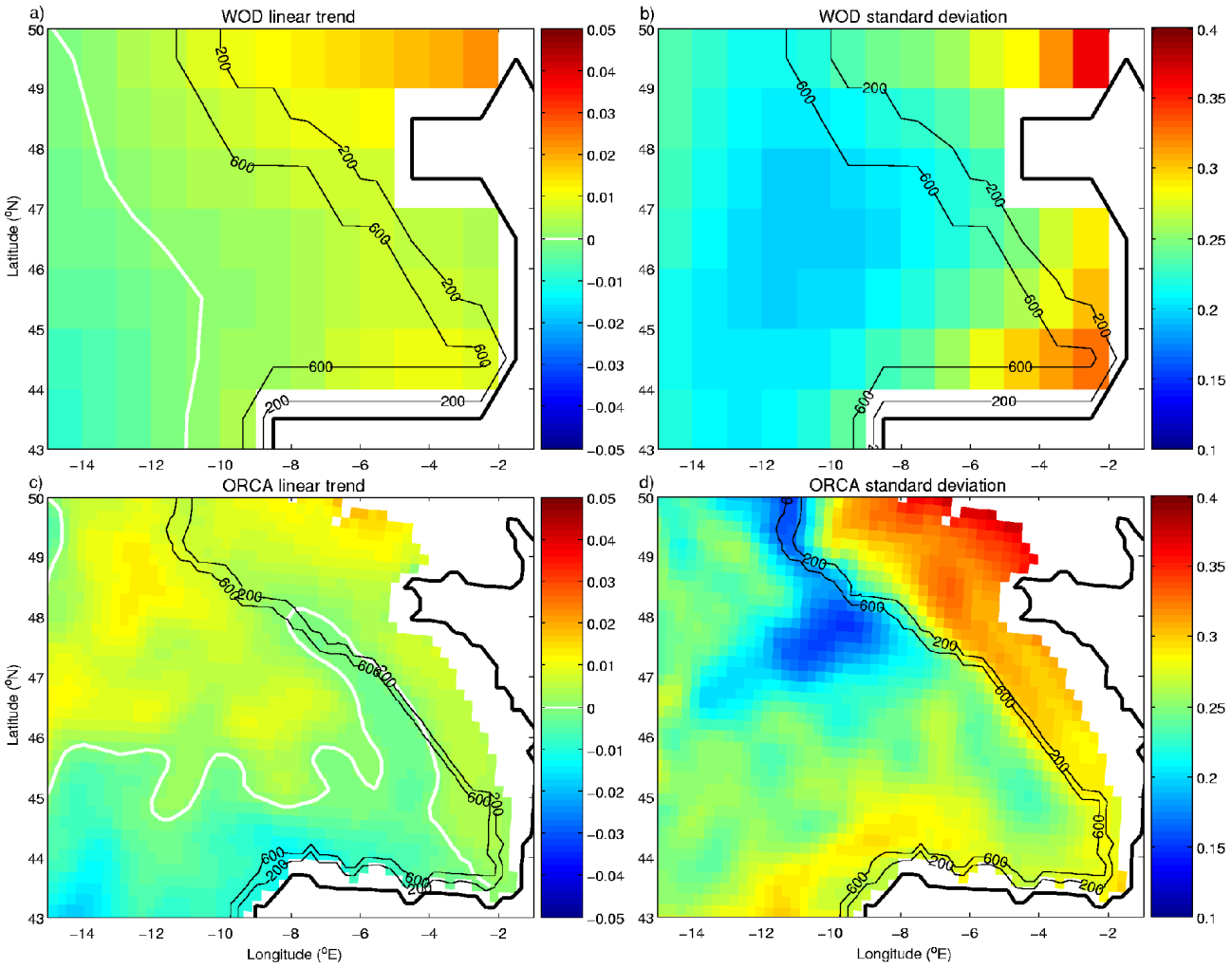


Fig. 4. Maps of linear trend in °C.year$^{-1}$ (a, c) and RMS of residuals in °C (b, d) of temperature annual means, during the period 1965-2003. (a, b) World Ocean Database analysis at the100-m depth; (c, d) ORCA simulation at the 94-m level. In the trend maps, the zero isoline is indicated with a white contour.

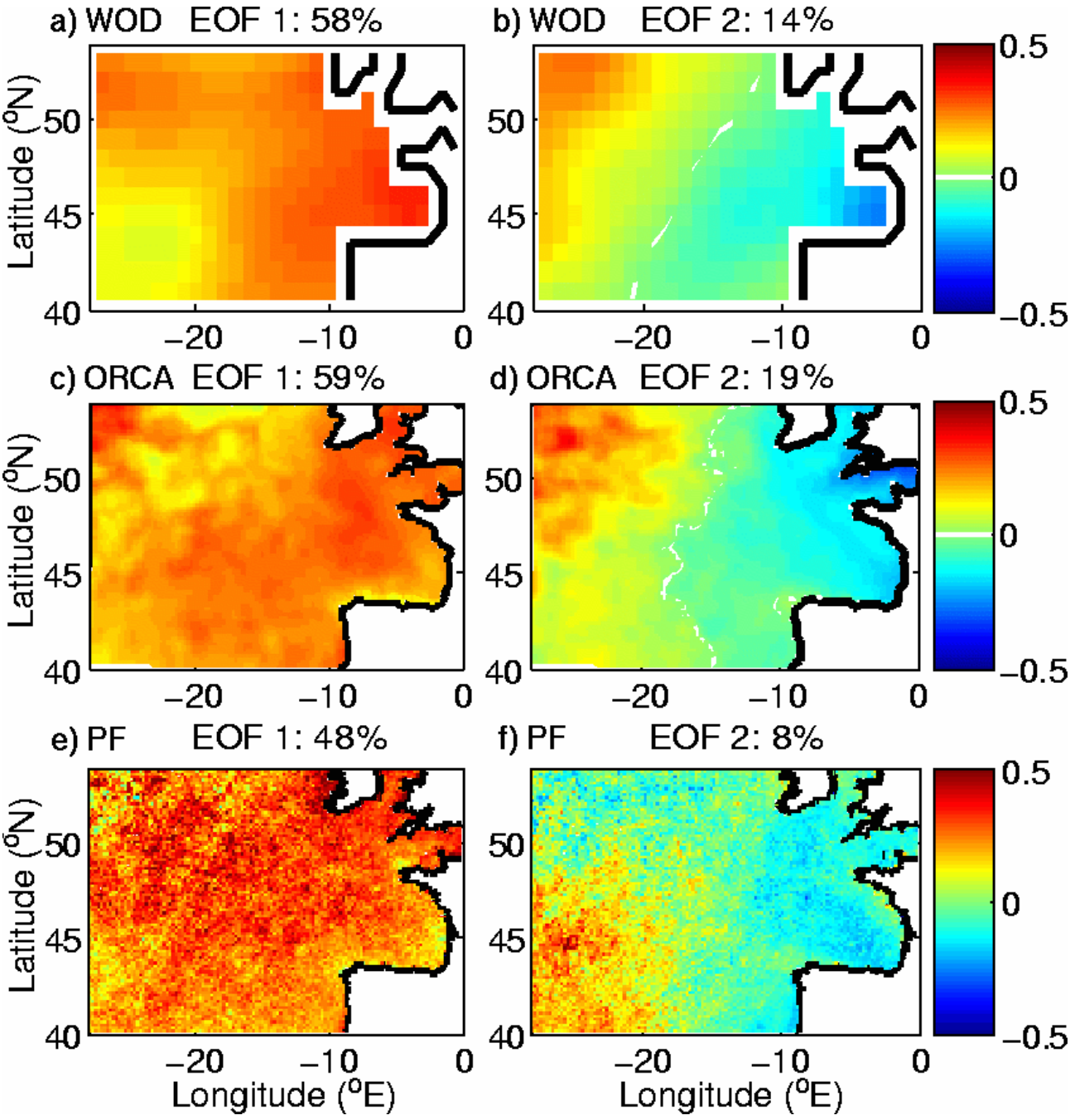


Fig. 5. Maps of the first two EOFs of annual mean temperature, during the 1985-2003 period, with the linear trend removed, computed over the displayed domain (40°N-54°N, 28°W-0°E). (a, b) World Ocean Database analysis at near-surface; (c, d) ORCA simulation at the 3-m level; (e, f) PathFinder v5 satellite SST. The percentages of explained variance are indicated above each map. The colour scale ranges from -0.5°C to 0.5°C for all datasets. The zero isolines are indicated in white, except for PathFinder because of its high in resolution.

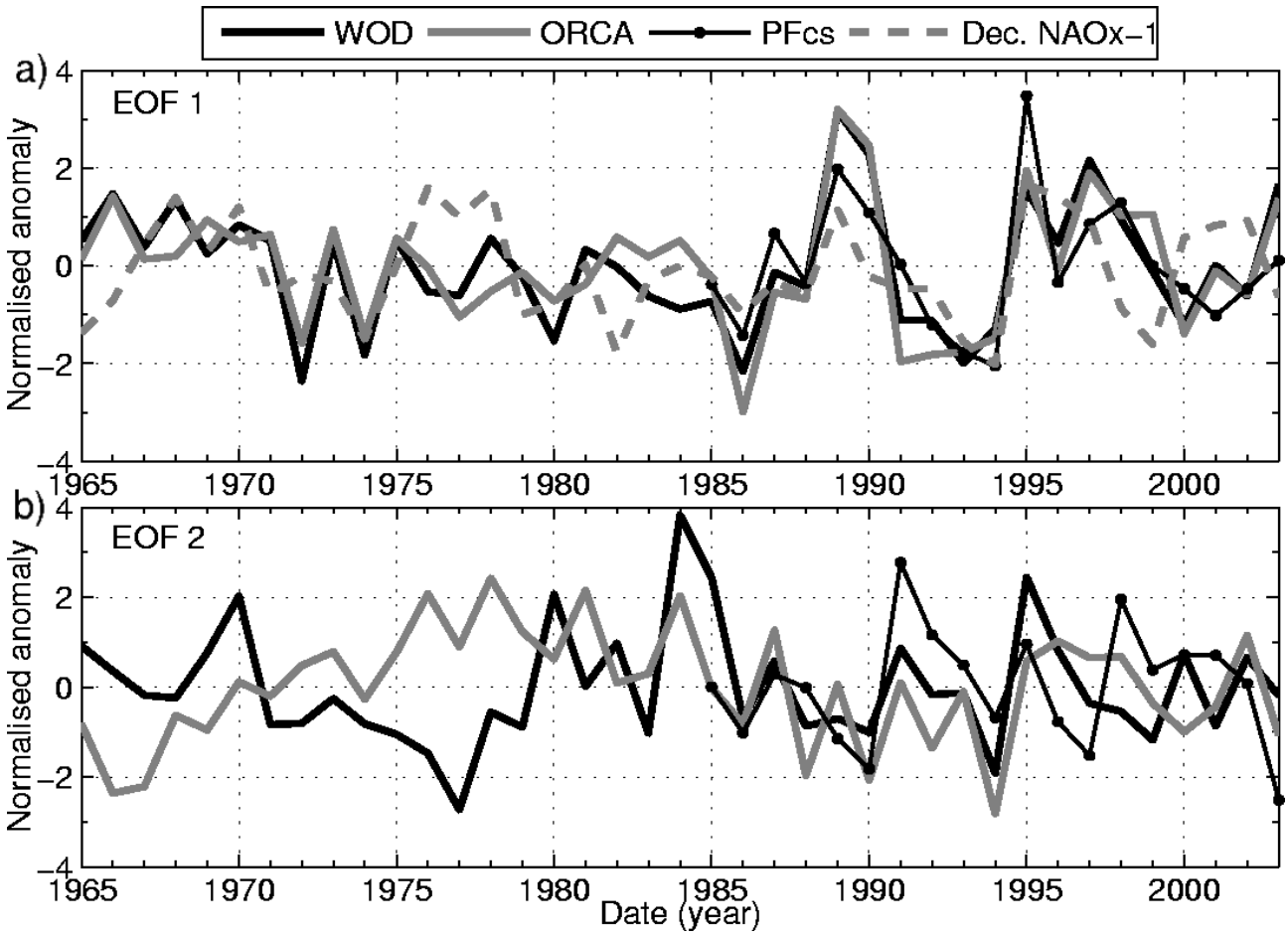


Fig. 6. Time-series of the first two EOFs of annual mean temperature, during the 1965-2003 period, with the linear trend removed, computed over the small domain (43°N-50°N, 15°W-1°W). Black thick line: World Ocean Database analysis at near-surface. Grey full line: ORCA simulation at the 3-m level. Black thin line: PathFinder v5 satellite SST (starting from 1985). Grey dashed line (in the top frame only): inverse NAO index in December of the previous year, from the Climate Prediction Center (http://www.cpc.noaa.gov/data/teledoc/nao.shtml). Each series is normalised so that its variance is unity.

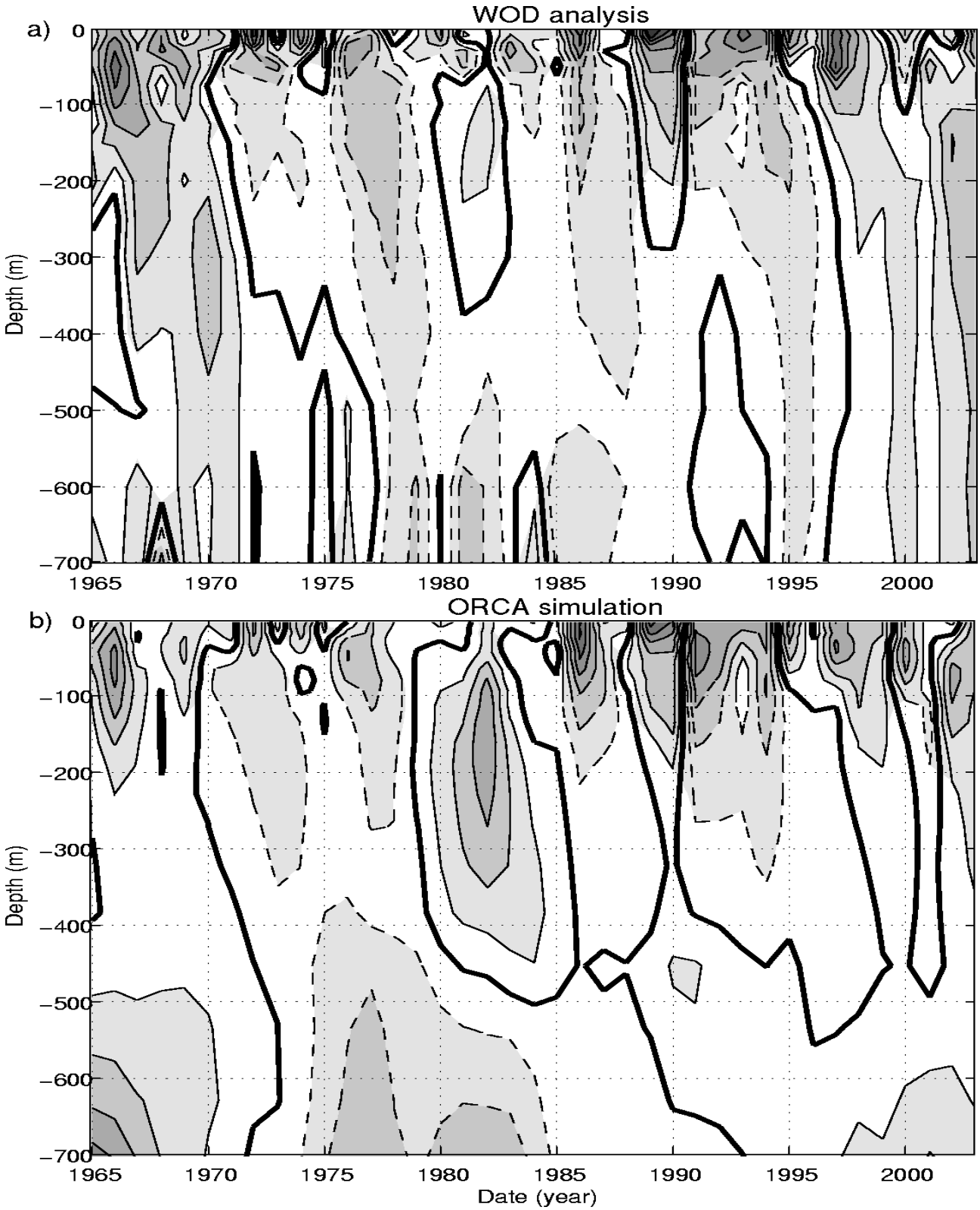


Fig. 7. Time-depth diagrams of temperature annual residuals, for years 1965 to 2003, averaged horizontally over the domain 43-50°N / 15°W-1°W. The data are the same as for the time-series in Fig. 2. (a) World Ocean Database, (b) ORCA simulation. The contour interval is 0.1°C; negative contours are traced with dashed lines and the 0 contour is traced with a thick line.

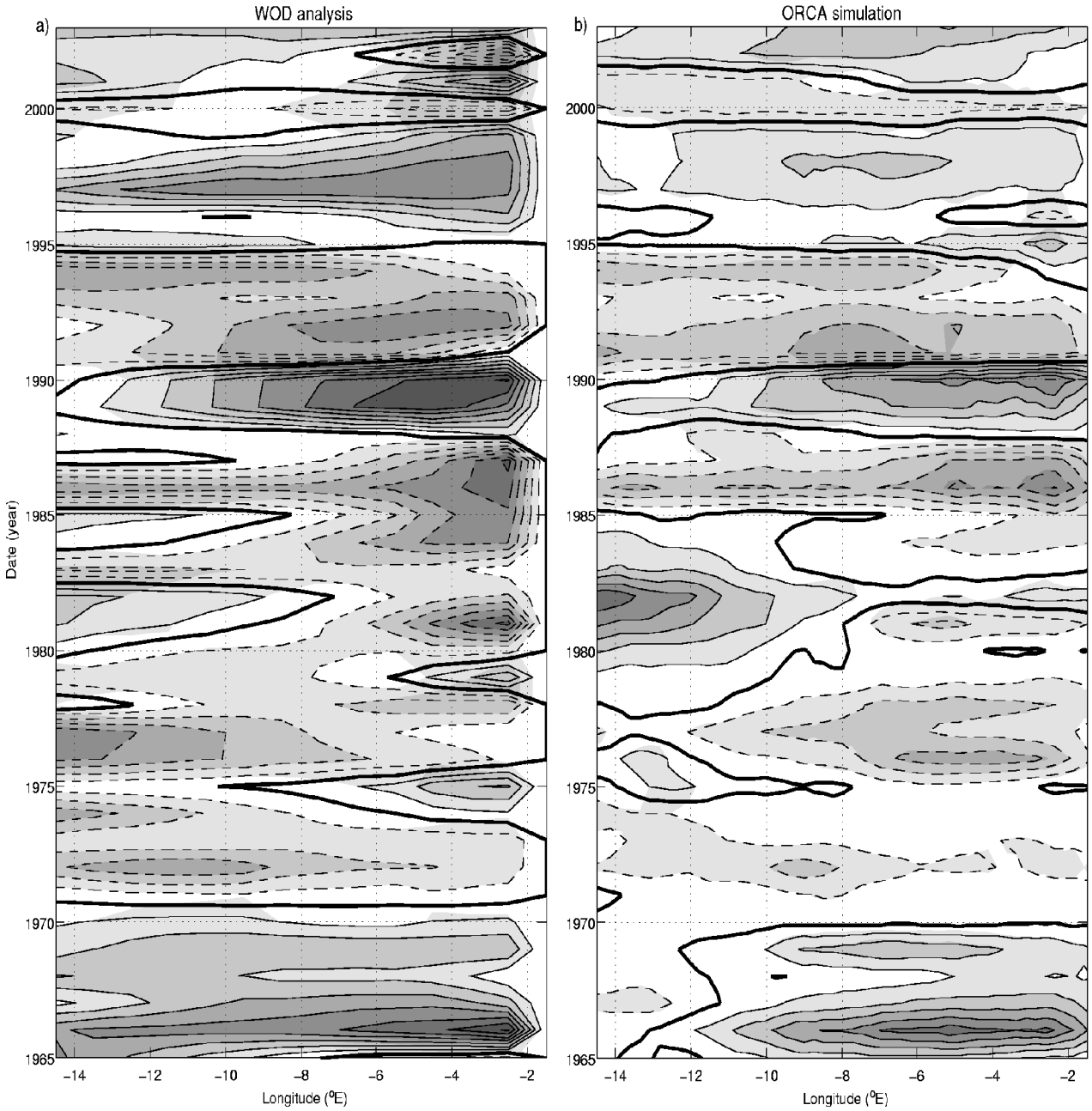


Fig. 8. Longitude-time diagrams of temperature annual residuals, for years 1965 to 2003, averaged meridionally over 43°N-50°N and vertically in the 0-200 m layer. (a) World Ocean Database, (b) ORCA simulation. The contour interval is 0.1°C; negative contours are traced with dashed lines and the 0 contour is traced with a thick line.

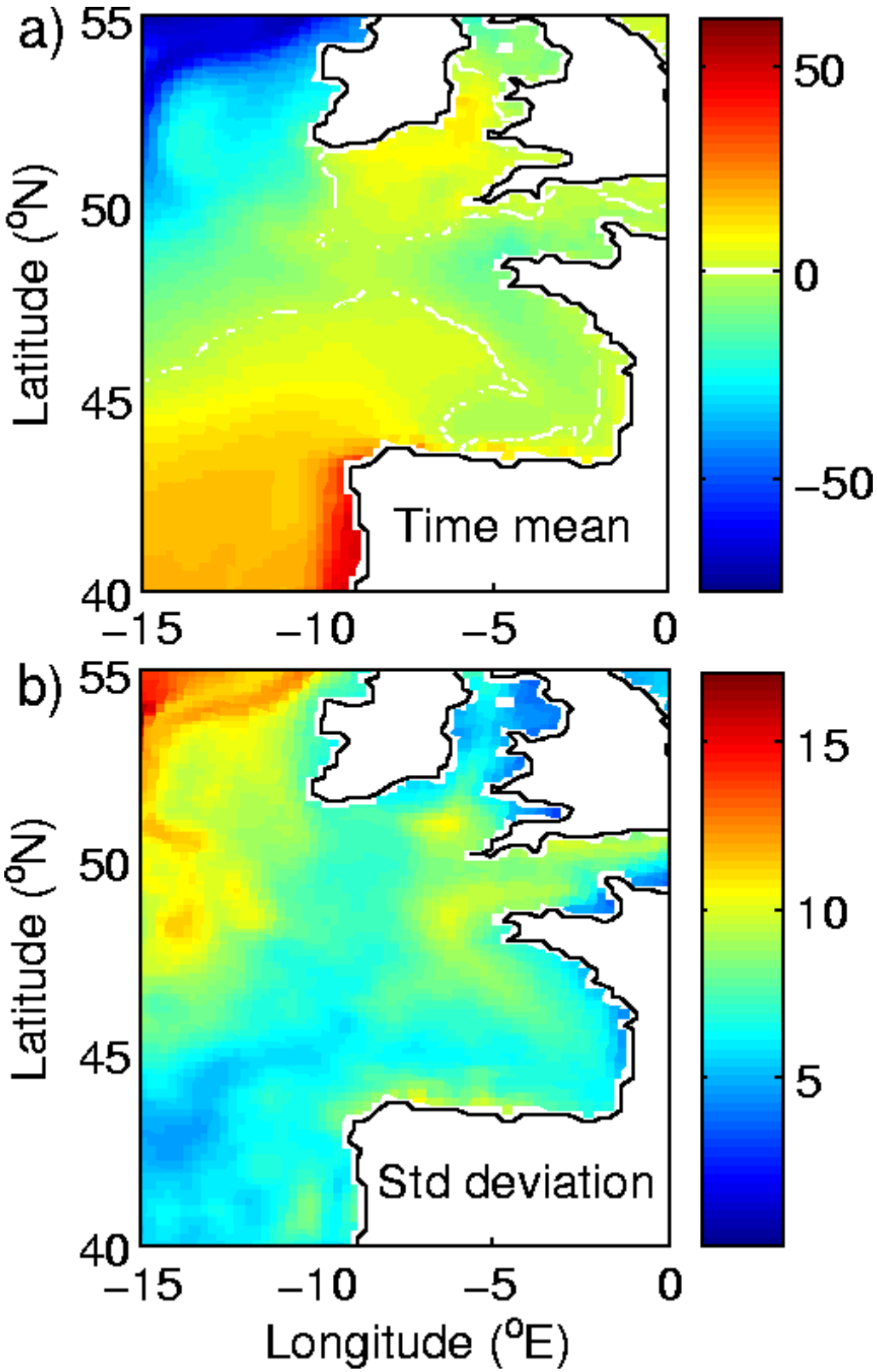


Fig. 9. Horizontal maps of net surface heat flux (in W.m$^{-2}$). (a) Average over the 1975-2004 period, (b) RMS of interannual anomalies. In the average map, the zero isoline is plotted as a white contour and positive values correspond to an heat input from the atmosphere to the ocean.

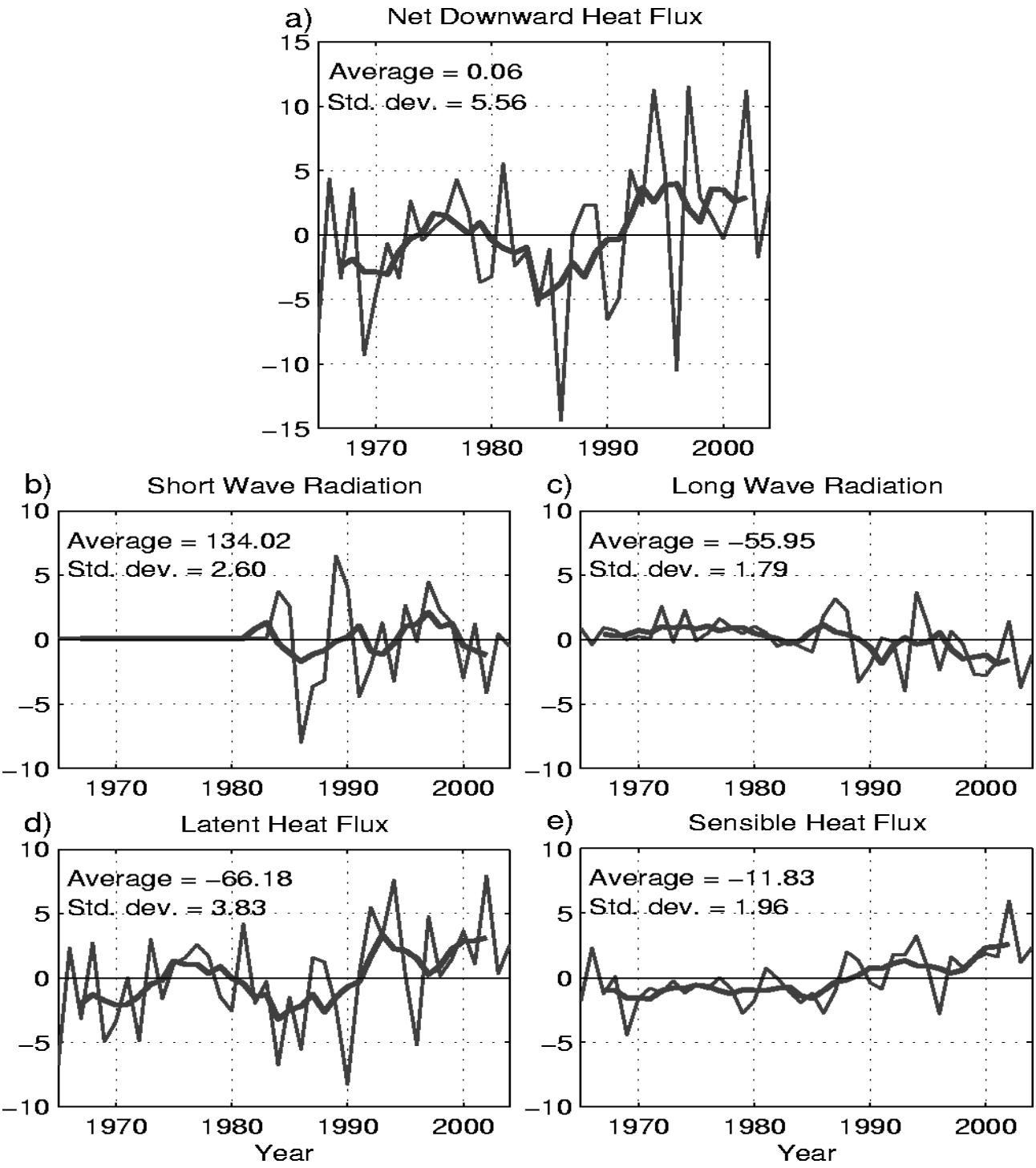


Fig. 10. Time-series of surface heat fluxes (in $W.m^{-2}$) averaged over the domain, as interannual anomalies (thin lines) and 5-year running means (thick line). (a) Net surface flux, (b) net solar radiation, (c) thermal radiation, (d) latent flux, (e) sensible flux. Positive values correspond to an heat input from the atmosphere to the ocean. For solar radiation, there are no interannual variations before 1980, because a climatology is used before this year. The mean and RMS values over the 1965-2004 period are indicated in the top-left corner of each plot.

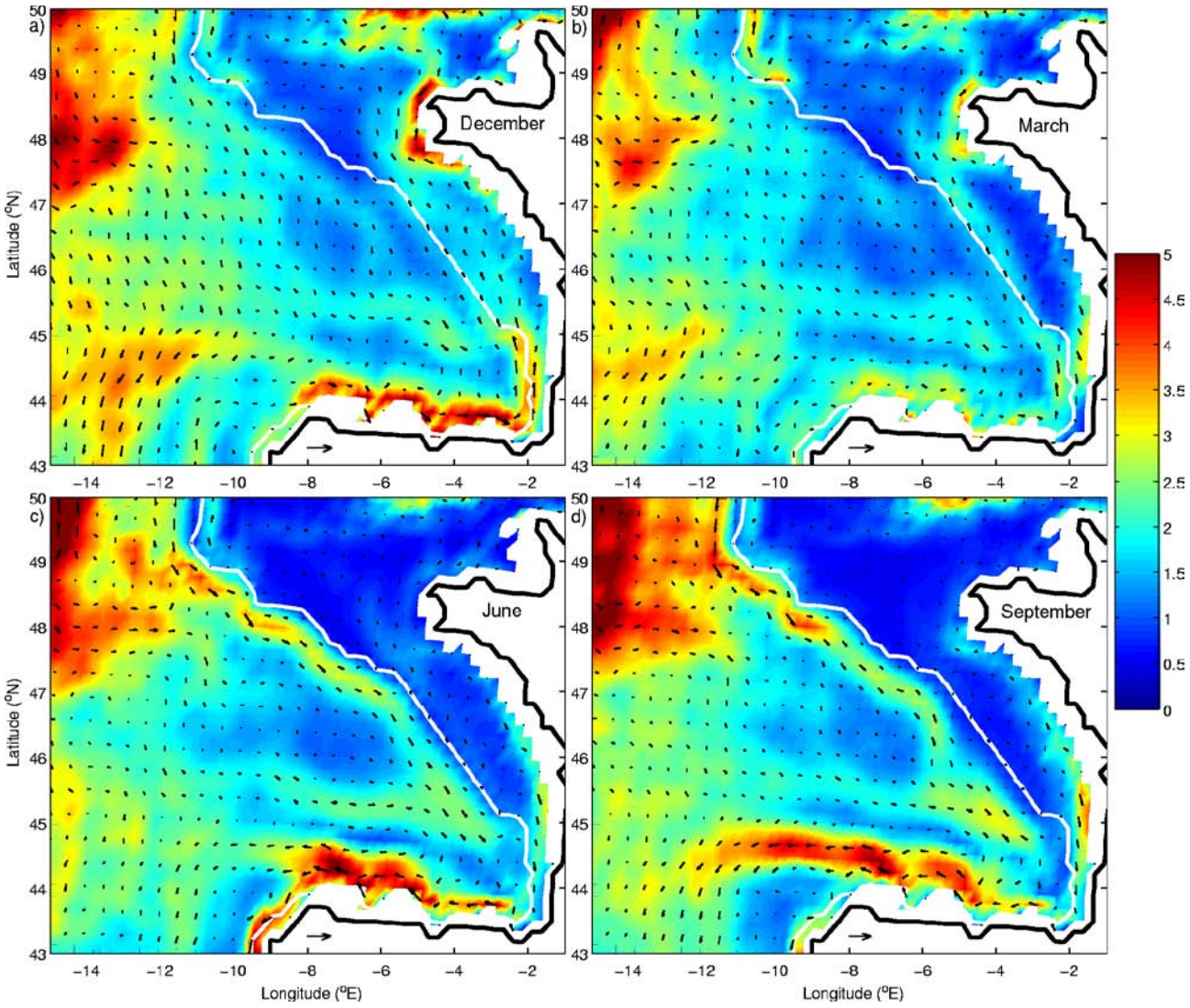


Fig. 11. Horizontal maps of simulated current velocity averaged in the 30-160 m layer, means of (a) December, (b) March, (c) June and (d) September, averaged over the 1965-2004 years. Arrows represent the mean current direction and colours represent the mean module of the velocity vector (systematically higher than the module of the mean velocity vector). The colour scale ranges from 0 to 5 cm.s$^{-1}$ and the reference vector at the bottom of each map represent a 10 cm.s$^{-1}$ zonal velocity. The 200 m isobath is plotted as a white line.

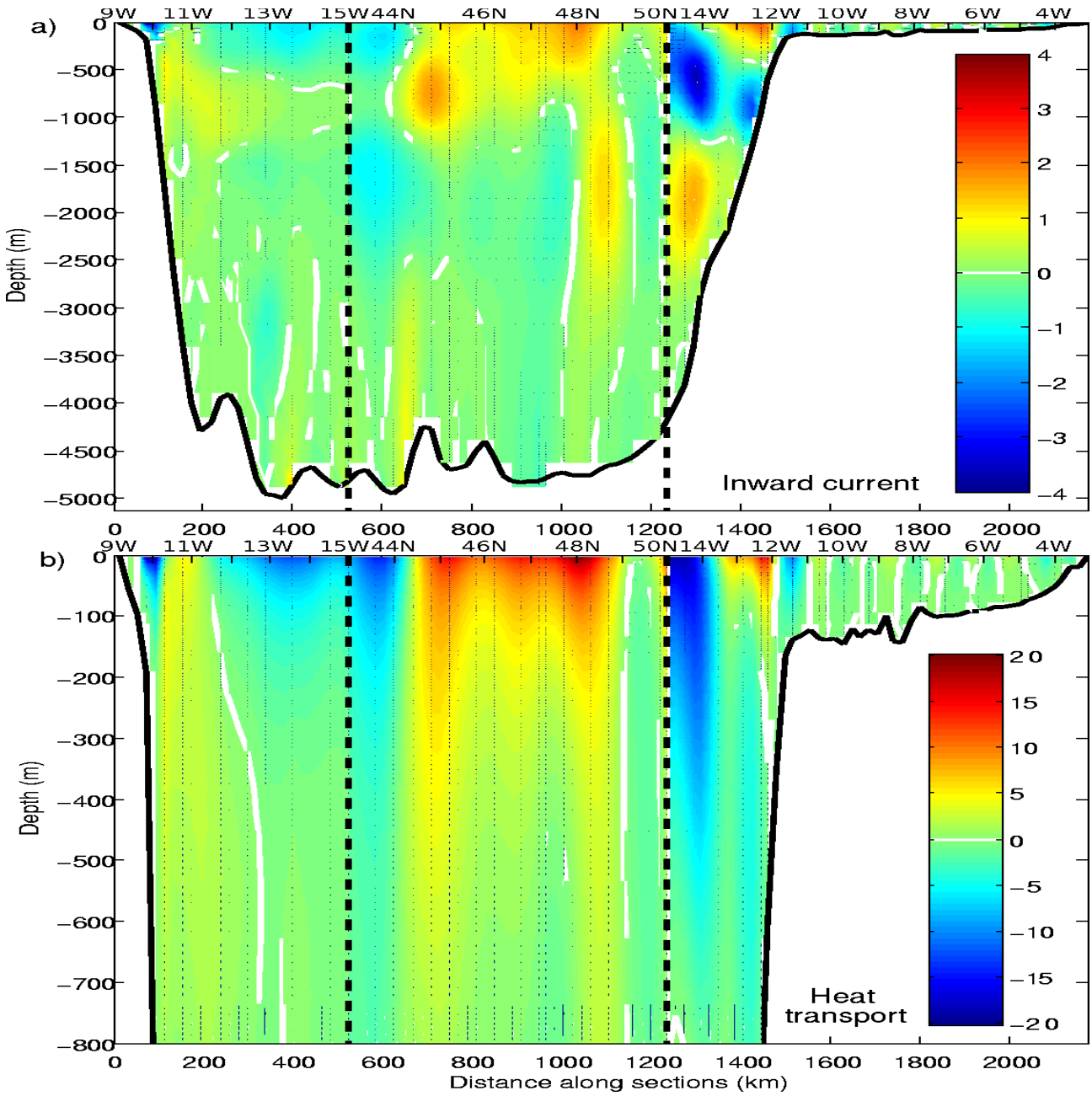


Fig. 12. (a) Vertical sections of simulated current velocity (in cm.s$^{-1}$) across the domain boundaries, averaged over the 1965-2004 years. (b) Heat transport (in TW) cumulated upward from the sea-floor to the surface, represented only in the upper 800 m. The three boundaries are plotted end-to-end, starting from the Iberian slope at 43°N to the left, continuing with the Atlantic section at 15°W, from south to north, and finishing with the Armorican slope and shelf at 50°N to the right. The vertical dashed lines mark the intersections at 43°N/15°W and 50°W/15°W. The vertical axis represents depths in meters from the surface. The upper horizontal axis represents longitudes and latitudes. The lower horizontal axis represents the distance in km from the start of the southern section. Positive values correspond to velocities or transport directed inward the domain.

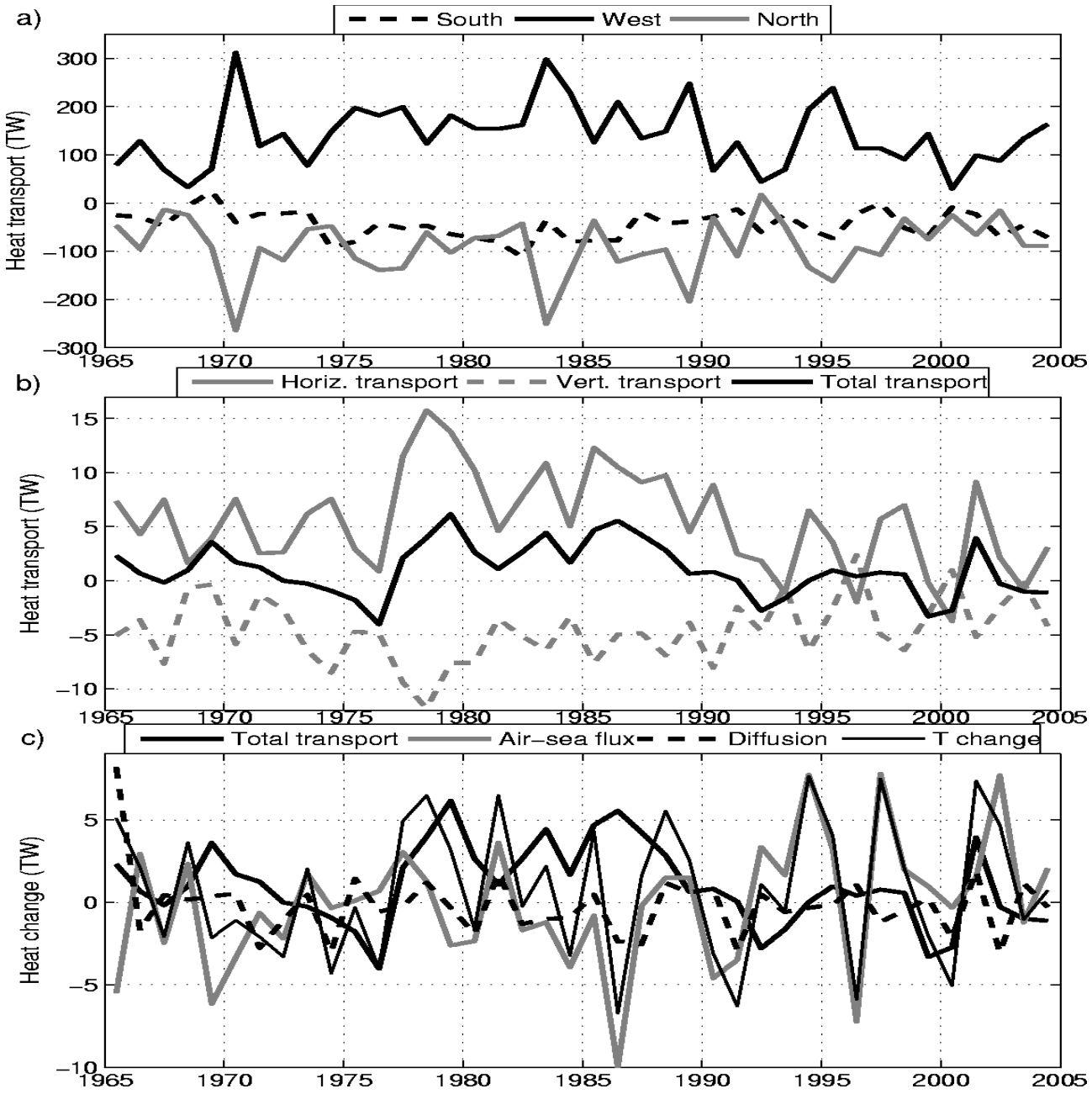


Fig. 13. Time-series of the simulated heat budget, integrated in the 0-800 m layer, in annual mean from 1965 to 2004. (a) Heat transport across the domain boundaries at 43°N (south), 15°W (west) and 50°N (north). (b) Horizontal transport (sum of the 3 transports in (a)), vertical transport (across the lower limit at 800 m), total transport (horizontal + vertical). (c) Total transport (same as in (b)), surface flux (from air to sea), temperature diffusion, depth-integrated temperature change (sum of all the budget terms). The line styles corresponding to each term of the budget are indicated at the top of each panel. All quantities are expressed in TeraWatts (1 TW = $10^{12}$ W). Positive (resp. negative) values indicate heat entering (resp. exiting) the domain.

Table 1. Statistics on observed and simulated temperature annual means at several depths, for years 1965 to 2003. Temperature data are averaged horizontally over the study area (43°N-50°N, 15°W-0°E). The selected depths correspond to levels in the World Ocean Database analysis, while the model outputs are taken at the nearest grid level. All quantities are expressed in °C, except for the linear trends, in °C per decade. All the trends are significant to more than 95%, except those indicated with a star (94%).

| Depth (m) | Period mean (° C) | | Linear trend (°C/ decade) | | RMS anomaly (° C) | | RMS residual (° C) | |
|---|---|---|---|---|---|---|---|---|
| | WOD | ORCA | WOD | ORCA | WOD | ORCA | WOD | ORCA |
| 5 | 14.48 | 14.50 | 0.19 | 0.10 | 0.40 | 0.29 | 0.33 | 0.26 |
| 50 | 12.98 | 13.22 | 0.23 | 0.10 | 0.37 | 0.26 | 0.26 | 0.23 |
| 100 | 12.00 | 12.19 | 0.19 | 0.10 | 0.28 | 0.22 | 0.19 | 0.19 |
| 200 | 11.65 | 11.83 | 0.14 | 0.04 | 0.22 | 0.13 | 0.15 | 0.12 |
| 400 | 11.13 | 11.41 | 0.04 | -0.02* | 0.11 | 0.07 | 0.10 | 0.07 |
| 600 | 10.57 | 10.29 | -0.04 | -0.10 | 0.12 | 0.18 | 0.12 | 0.14 |

Table 2. Statistics on observed and simulated sea surface temperature annual means, for years 1985 to 2003. The data processing is the same as for Tables 1 and 3. The mean differences (or biases) are computed in the sense ORCA minus WOD and PathFinder minus WOD. All quantities are expressed in °C, except for the linear trend, in °C per decade, the trend significance and the time correlation, in percent. All the correlation coefficients are significant to more than 99%.

| Statistic | WOD | ORCA | PathFinder |
|---|---|---|---|
| Mean (°C) | 14.69 | 14.59 | 14.46 |
| Trend (°C/decade) | 0.30 | 0.22 | 0.37 |
| Trend significance (%) | 91 | 86 | 96 |
| RMS anomaly (°C) | 0.43 | 0.36 | 0.43 |
| RMS residual (°C) | 0.39 | 0.34 | 0.38 |
| Mean difference (°C) | - | -0.10 | -0.23 |
| RMS difference (°C) | - | 0.13 | 0.12 |
| Residuals correlation (%) | - | 96 | 96 |

Table 3. Statistics of comparison between observed and simulated temperature annual means at several depths, for years 1965 to 2003. The data processing is the same as for Table 1. The mean differences (or biases) are computed in the sense simulation minus observations. The RMS differences and the correlations are computed from the annual residuals (i.e. with the linear trend removed). Differences are expressed in °C, while the time correlation is expressed in percent. All the correlation coefficients are significant to more than 95%, except those indicated with a star (89%).

| Depth (m) | Mean difference (°C) | RMS difference (°C) | Residuals correlation (%) |
|---|---|---|---|
| 5 | 0.02 | 0.18 | 91 |
| 50 | 0.24 | 0.20 | 82 |
| 100 | 0.19 | 0.14 | 87 |
| 200 | 0.17 | 0.16 | 62 |
| 400 | 0.28 | 0.13 | 26* |
| 600 | -0.27 | 0.15 | 52 |

Table 4. Budgets simulated during the period 1965 to 2004, in the study area (43°N-50°N, 15°W-1° W) and in the upper 800 m. From left to right, the columns correspond to the mean volume budget, the mean heat budget and its RMS variation. Volume components are expressed in milliSverdup (1 mSv = 1000 $m^3.s^{-1}$) and heat components are expressed in TeraWatts (1 TW = $10^{12}$ W). All quantities are computed as inputs to the oceanic domain. The horizontal transport is the sum of the transports across the three lateral boundaries (south, west and north). The total transport is the sum of horizontal and vertical transports. The diffusion term is obtained as the difference between the content change and the other budget terms.

| Budget term | Volume input (mSv) | Heat input (TW) | Heat RMS (TW) |
|---|---|---|---|
| Transport south | -741 | -45 | 29 |
| Transport west | 2901 | 141 | 66 |
| Transport north | -2043 | -90 | 59 |
| Lateral transport | 116.75 | 5.61 | 4.42 |
| Vertical transport | -116.87 | -4.57 | 2.94 |
| Total transport | -0.12 | 1.04 | 2.47 |
| Heat flux | - | -0.09 | 3.78 |
| Freshwater flux | 0.38 | -0.02 | 0.09 |
| Diffusion | - | -1.17 | 0.84 |
| Content change | 0.20 | -0.24 | 3.86 |

Table 5. Interdecadal variations of the simulated heat budget during the period 1965 to 2004, in the study area (43°N-50°N, 15°W-1°W) and in the upper 800 m. The mean budget during each decade from 1965-1974 to 1995-2004 is indicated in a column, from left to right. All terms are expressed in TeraWatts (1 TW = $10^{12}$ W). The calculation conventions are the same as for Table 4. The heat content change is the difference between the end and the beginning of each decade, while the heat content trend is calculated by linear regression over each decade.

| Heat budget term (TW) | 1965-1974 | 1975-1984 | 1985-1994 | 1995-2004 |
|---|---|---|---|---|
| Transport south | -28 | -67 | -43 | -44 |
| Transport west | 118 | 188 | 137 | 121 |
| Transport north | -85 | -113 | -87 | -75 |
| Lateral transport | 5.11 | 8.28 | 6.48 | 2.56 |
| Vertical transport | -4.21 | -6.44 | -5.04 | -2.57 |
| Total transport | 0.90 | 1.84 | 1.44 | -0.01 |
| Heat flux | -1.36 | -0.31 | -0.34 | 1.64 |
| Freshwater flux | 0.01 | -0.06 | -0.03 | 0.00 |
| Diffusion | -1.27 | -1.09 | -1.01 | -1.30 |
| Heat content change | -1.72 | 0.38 | 0.06 | 0.33 |
| Heat content trend | -1.94 | 1.04 | -0.29 | 0.51 |